

Structural, optical and electrical properties of Mn-doped ZnFe₂O₄ synthesized using sol-gel method

Harshpreet Cheema

Banasthali Vidyapith: Banasthali University

Vedika Yadav

Banasthali Vidyapith: Banasthali University

Ram Sundar Maurya

Banasthali Vidyapith: Banasthali University

Varsha Yadav

Banasthali Vidyapith: Banasthali University

Aditya Kumar

University of Allahabad

Nidhi Sharma

Banasthali Vidyapith: Banasthali University

Parvej Ahmad Alvi

Banasthali Vidyapith: Banasthali University

Upendra Kumar (✉ upendra.bhu512@gmail.com)

Indian Institute of Information Technology Allahabad <https://orcid.org/0000-0001-9200-0048>

Research Article

Keywords: Mn-doped ZnFe₂O₄, XRD, Raman Spectroscopy, DC conductivity, Arrhenius plot.

Posted Date: June 23rd, 2021

DOI: <https://doi.org/10.21203/rs.3.rs-485344/v1>

License:  This work is licensed under a Creative Commons Attribution 4.0 International License.

[Read Full License](#)

Structural, optical and electrical properties of Mn-doped ZnFe₂O₄ synthesized using sol-gel method

Harshpreet Cheema¹, Vedika Yadav¹, Ram Sundar Maurya¹, Varsha Yadav¹, Aditya Kumar²,
Nidhi Sharma¹, Parvej Ahamad Alvi¹, Upendra Kumar^{3*}

¹Department of Physical Sciences, Banasthali Vidyapith, Banasthali-304022, Rajasthan, India

²Center of Material Sciences, University of Allahabad, Prayagraj-211002, India

³Department of Applied Sciences, Indian Institute of Information Technology, Allahabad, Devghat, Jhalwa,
Prayagraj-211015, India

Corresponding author: upendra.bhu512@gmail.com*

Abstract

Samples with doping of Mn (0, 2, and 4%) in ZnFe₂O₄ were prepared by sol-gel chemical route at 80°C. X-ray powder diffraction and Raman spectrum analysis were used to determine the preliminary phase of obtained samples. W-H and SSP plots were used to determine the crystallite size and micro-strain of samples. Using zeta potential and scanning electron microscope, the surface charge and morphology of the prepared samples were studied. The optical bandgap of sample suggested that it was semiconducting. The dielectric characteristics of samples were examined as a function of temperature at various frequencies (1 KHz, 10 KHz, 100 KHz, and 1 MHz) (60-600°C). Dielectric study revealed the presence of interfacial and orientational polarization, with dielectric constants and dissipation factors ranging from (0.7-460) to (0.3-0.8), remain thermally stability up to 300°C. In samples ZF-0, ZF-2, and ZF-4, the thermal dependence of DC conductivity demonstrates Arrhenius transport with one, two, and three regions of conduction, respectively. The sources of charge carrier in samples were $V_o^{\cdot\cdot}$, e' and dipole defects ($V_o^{\cdot\cdot} - 2Fe^{2+}_{Fe^{3+}}$) and ($2Mn^{3+}_{Zn^{2+}} - 2Fe^{2+}_{Fe^{3+}}$). The current work could help identify possible applications in semiconductor devices, thermally stable capacitors, and as mixed ionic electronic conductors in solid oxide fuel cells.

Keywords: Mn-doped ZnFe₂O₄; XRD; Raman Spectroscopy; DC conductivity; Arrhenius plot.

* **Corresponding author:** Upendra Kumar

Email: upendra.bhu512@gmail.com

Introduction:

Polycrystalline ferrites were classified as good magnetic semiconductors having low electrical conductivity and eddy currents, that play an essential role in various technological applications from microwave to radio wave frequencies [1, 2]. Ferrites also belong to a special class of ceramic materials that exhibit ferromagnetic nature at room temperature [3]. Among the several spinel ferrites, MFe_2O_4 ($M=Zn, Mn, Co, Ni$), $ZnFe_2O_4$ exhibits particularly intriguing features due to the diamagnetic nature of Zn^{2+} and the ferrous behavior of Fe (Fe^{2+} and Fe^{3+}) ions, which have highly physical and chemical stability [4]. $ZnFe_2O_4$ belongs to cubic spinel group crystallized under $Fd\bar{3}m$ space group with lattice constant $a=8.35 \text{ \AA}$ [5]. Substitutional doping in the $ZnFe_2O_4$ lattice can be done at either the Zn-site, the Fe-site, or both sites, which has been studied for various applications such as gas sensors, electromagnetic wave absorbing materials, photocatalyst, electrode materials for supercapacitors, proton conductor in solid oxide fuel cells, and electrode for Li-ion battery applications [2, 6–12].

$ZnFe_2O_4$ has tetrahedral distribution of cations formed by Zn-sites and an octahedral distribution of cations formed by Fe-sites. The octahedral site of Fe distributed by Fe^{2+}/Fe^{3+} has different values of crystal field stabilization energy (CFSE) [13]. The value of CFSE has been reported to be higher for an octahedral site than for a tetrahedral site in spinel ferrite. The distribution of tetrahedral and octahedral sites among Zn^{2+} , Fe^{3+}/Fe^{2+} in the crystal structure of $ZnFe_2O_4$ is completely random [6]. The CFSE is controlled by the ligand environment, which has a significant impact on several dielectric and electrical properties of $ZnFe_2O_4$ [14]. These intriguing features of $ZnFe_2O_4$ compelled us to use it in the current study. Several findings mentioned in the literature suggest $ZnFe_2O_4$ as a multifunctional material with various modifications. Cr doped $ZnFe_2O_4$ synthesized by co-precipitation method has been used for semiconductor devices, high frequency transformer core, rod antennas and radio-frequency coils

application [14]. Co modification of MnFe_2O_4 has been used in the microwave industry for applications such as radar absorbing materials (RAM), satellite communication, anechoic chambers, and microwave protection of living bodies [15]. According to the literature review including these two articles, the substitution of Mn at the Zn-site makes it more multifunctional than its solo phase. Sidra Zavar et al. produced Mn-modified ZnFe_2O_4 by a wet chemical-based auto-combustion process, which they found useful in EM wave shielding [16]. Hema et al. synthesized a solid solution of $\text{Zn}_{1-x}\text{Mn}_x\text{Fe}_2\text{O}_4$ using a simple one-pot microwave combustion process using urea as the fuel, which exhibits superparamagnetism within $0 \leq x \leq 0.4$ and ferromagnetism within $0.6 \leq x \leq 1.0$; it is also a suitable catalyst for the oxidation of benzyl alcohol into benzaldehyde [17]. Ying Zhao et al. produced Mn-doped ZnFe_2O_4 by calcining at different temperatures ranging from 400°C to 600°C using the sol-gel method; it exhibits good catalytic ozonation suitable for water purification [18]. R. D. Raland et al. used a simple coprecipitation method to prepare Mn doped ZnFe_2O_4 and found it to be a superparamagnetic materials suitable for magnetic hyperthermia application [19]. Mn modification in ZnFe_2O_4 nanoparticles have been intensively researched as anode materials for lithium-ion batteries [20]. A careful review of the literature revealed that no systematic investigations on the detailed investigation of the structure and electrical characteristics of Mn-doped ZnFe_2O_4 had been conducted. As a result, studies on the structural and electrical properties of Mn-modified ZnFe_2O_4 should be required not just for application purposes but also for a fundamental knowledge of the solid-state physics involved.

Furthermore, the processing parameters have a significant impact on the development and qualities of materials [15]. There are several methods reported in the literature for the synthesis of ZnFe_2O_4 nanomaterials such as solid state [21], pyrolysis [6], coprecipitation [22],

microemulsion [23], sol-gel self-propagating combustion [24], hydrothermal [25], mechanical activation [26], rapid quenching [27], solvothermal [21], combustion [28] and precipitation method [29]. Every studied method has its own set of advantages and disadvantages. Because of its simple experimental setup, high crystallinity, exceptional purity, and uniform particle distribution in a short processing duration at a low temperature, sol gel is one of the best and most appealing method [30].

As a result, in order to achieve the aforementioned aim, the Mn-doped ZnFe_2O_4 sample was synthesized using sol-gel chemical route at 80°C . X-ray diffraction (XRD) and Zeta potential analyses were used to identify the phase and surface charge properties of materials. Further the incorporation of Mn-doping at Zn-site was probed using Raman analysis. The cylindrical pellets of samples sintered at 700°C were projected for microstructure and electrical properties analysis. The DC conductivity of samples has been recorded to explore their transport properties. The present study focuses on the synthesis of Mn-doped ZnFe_2O_4 to investigate its properties for potential application in semiconductor and nano-devices.

Experimental Procedure:

Materials

In order to synthesize Mn-modified ZnFe_2O_4 , zinc nitrate $\text{Zn}(\text{NO}_3)_2 \cdot 6\text{H}_2\text{O}$, iron nitrate $\text{Fe}(\text{NO}_3)_3 \cdot 9\text{H}_2\text{O}$, Manganese nitrate $\text{Mn}(\text{NO}_3)_2 \cdot 4\text{H}_2\text{O}$, and citric acid ($\text{C}_6\text{H}_8\text{O}_7$) were procured as raw material from Alfa-Aesar. The ammonia solution and acetone bought from Merck, were used for precipitation and cleaning purposes respectively. The emery paper of different grades (1/0, 2/0, and 3/0), silver paste, and other reagents have been used without further purification.

Synthesis of Mn-doped ZnFe_2O_4

$Zn_{1-x}Mn_xFe_2O_4$ with $x=0, 0.02,$ and 0.04 were prepared by Sol-Gel route. Initially, the raw materials and citric acid were weighed in a stoichiometric ratio and prepared separately in deionized (DI) water, with the raw materials and citric acid having a molar ratio of 1:2. Using litmus paper, the pH of the solution was tested several times and found to be in the range of 3-5. Furthermore, by adding an ammonia solution, the pH of the obtained solution was adjusted to a range of 9-10. After that, the final solution was placed on a magnetic hot plate with constant stirring and held at 80°C until it dried into a gel. After 2 hours of constant stirring, the dried gel ignited and turned into a fine brown powder. The powder was then carefully ground in an agate mortar to make a homogeneous powder. Figure 1 shows a pictorial representation of the steps involved in nanopowder synthesis. To confirm the formation of single phase, the final powder was subjected to a variety of characterization techniques. The obtained powder was uniformly mixed with 2% polyvinyl alcohol (PVA) and compact cylindrical pellets of 12 mm diameter and 1.5 mm thickness were made to perform the electrical measurement. The pellets were then sintered at 700°C for 6 hours before being washed with emery paper of various qualities (1/0, 2/0, 3/0) and acetone. Silver paste was also used to make a conducting contact on both the surface of the pellets. To make a parallel plate capacitor, the silver coated pellets were fired at 300°C for 25 minutes. The morphology and electrical characterization of the silver-coated pellets were then recorded.

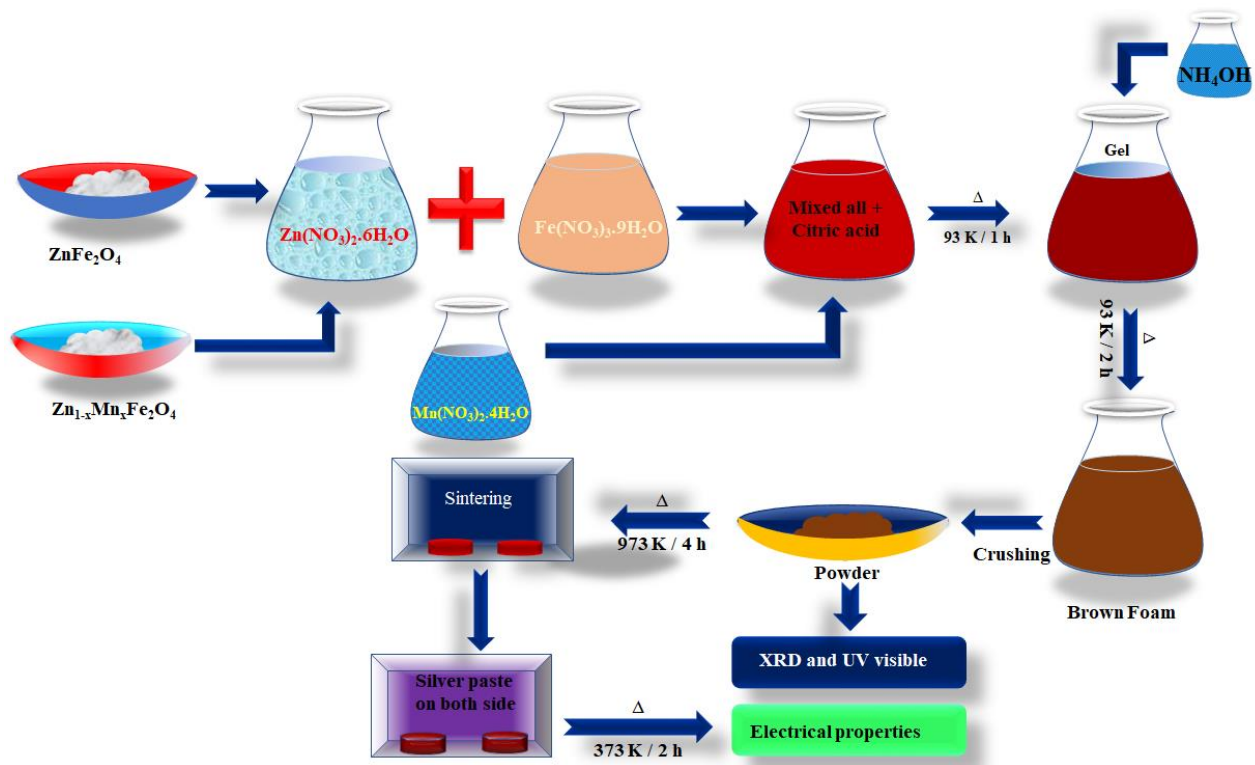


Figure 1: Synthesis of $Zn_{1-x}Mn_xFe_2O_4$ using Sol-Gel chemical route with all steps incorporated during preparation.

Characterization techniques:

Phase identification and structure determination of samples were performed by X-ray diffraction (XRD) analysis with the help of X-ray powder diffractometer (Miniflex Rigaku) employing $CuK\alpha$ radiation ($\lambda=0.154$ nm) within the angular range of $2\theta = 20-80^\circ$. The hydrodynamic particle size and zeta potential of samples were recorded using Malvern Nano Z.S. instrument (Malvern Instrument, Worcestershire). Using a Raman spectrophotometer, the Raman spectrum of samples in the wave-number range of $50-1000$ cm^{-1} was recorded at room temperature (T64000, Jovin-Yvon Horiba). The optical band gap of prepared samples was obtained from UV-Vis. spectra using a UV-Vis spectrophotometer (V-770, Jasco Japan). A high-resolution scanning electron microscope was used to examine the surface morphology of sintered pellets (ZEISS,

model EVO-18 research). Using a high-precision LCR meter (Wayne Kerr), the dielectric properties of silver-coated pellets were investigated over a broad temperature range (60–600 °C) and at various frequencies (1 KHz, 10 KHz, 100 KHz, 1 MHz). The electrical conductivity of the same pellets was calculated using a 2-probe system, which involved applying a voltage of 5 V across the pellets using a constant-voltage source and an Electrometer (Model 617, Keithley).

Results and Discussion:

In the present investigation, the samples with different doping concentrations with $Zn_{1-x}Mn_xFe_2O_4$ ($x=0, 0.02, \text{ and } 0.04$) have been referred as ZF-0, ZF-2, and ZF-4 respectively. For example, ZF-2 represents the sample $Zn_{0.98}Mn_{0.02}Fe_2O_4$ and so on.

Characterization of $Zn_{1-x}Mn_xFe_2O_4$ powder:

Structural Characterization of $Zn_{1-x}Mn_xFe_2O_4$:

Powder X-ray diffraction analysis was used to identify the phases of the prepared samples, as shown in Figure 2. All the diffraction peaks in the XRD pattern correspond to the cubic spinel group of $ZnFe_2O_4$ crystallographic open database (COD) file no. 1010130 [5]. However, the width and the sharpness of peaks changed significantly with Mn substitution in $ZnFe_2O_4$. Further, the incorporation of Mn at Zn^{2+} site has been probed by enlarging the XRD peaks observed at 34.90° . The position of XRD peak was found to be shifted towards lower angle for ZF-2 and somewhat towards the higher angle for ZF-4. Zn ionic radii at tetrahedral sites is 0.6 Å, which is smaller than Mn^{2+} ionic radii (0.66 Å). Based on the difference in value of ionic radii it is expected that XRD peak may shift towards lower angle that is contradictory for sample ZF-4. There might be two possibilities, either the Mn is present in more than one valence state such as Mn^{3+} (0.645 Å) or Fe may exist in more than one valence state Fe^{3+} (0.645 Å) and Fe^{2+} (0.78 Å) [31]. Conventionally, in $ZnFe_2O_4$, Zn exhibit Zn^{2+} valence state and Fe exhibit Fe^{3+} valence

state; since the prepared samples were single phase so the conversion of Fe in Fe^{2+} is impossible while presence of Mn in Mn^{3+} is favorable. Presence of Mn^{3+} at Zn site leads to slight shift in position of peak towards higher angle due to its lower ionic radii than Zn^{2+} . According to Bragg's law, the angular position $\theta \propto 1/d$, where d is interplanar spacing, that indicates a shift in angular position towards higher angle with lower ionic radii and towards lower angle by incorporation of higher ionic radii [31, 32].

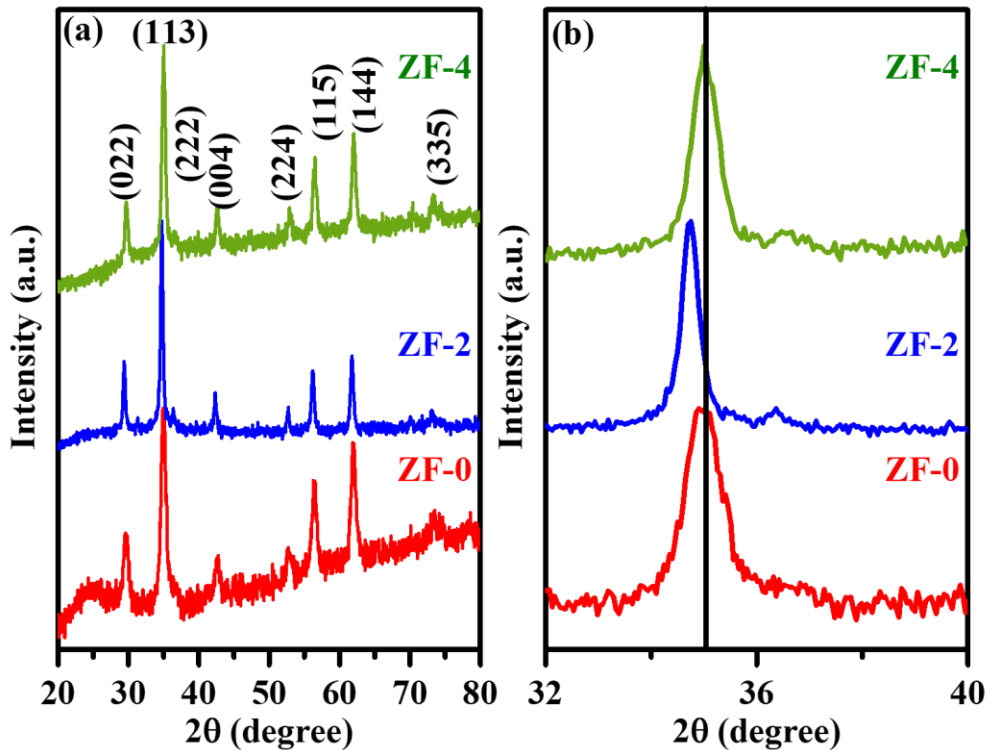


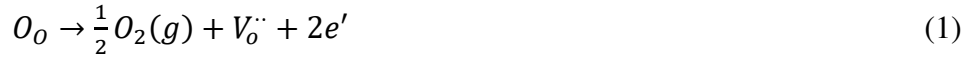
Figure 2: (a) X-ray diffraction pattern of $\text{Zn}_{1-x}\text{Mn}_x\text{Fe}_2\text{O}_4$ samples, (b) Enlarge view of XRD pattern.

Rietveld refinement analysis

The influence of Mn-doping on structural parameters is investigated by performing Rietveld refinement on XRD data using the FullProf Software suite, and the refinement pattern of all samples is shown in Figure 3. (a-c). To accomplish the refinement, the crystal structure is considered as cubic and space group $Fd\bar{3}m$. Interpolation between a set of background points

with refinable heights is used to describe the background of XRD pattern. However, the XRD peak form has been represented as pseudo-Voigt. The scale factor, zero correction, background, half-width parameters (u, v, w), lattice parameters (a, b, c), angle (α, β, γ), positional coordinate (x, y, z) and the thermal parameters (B) were varied during the process of refinement, while the occupancy parameters for all the ions keep fixed. Table 1 displays the structural parameters acquired after refinement, such as the lattice parameter, unit cell volume, bond lengths, bond angles, and other pertinent parameters. After the repeated refinement, the values of the fitting parameters R_p , R_{wp} , R_{exp} , and χ^2 were obtained and given in Table 1. The quality of fitting has been analysed by calculating a parameter called goodness of fit, $S = R_{wp}/R_p$ and their values range from 1.26-1.39, indicating that the parameters derived via refinement are relevant [33]. Table 1 shows that the value of the lattice parameter found for the undoped sample is slightly higher than the reported value [6]. This could be owing to variations in the processing parameters (such as time, temperature, pressure, and so on) used during sample preparation in the current study. Furthermore, in order to comprehend the variation of structural parameters, the crystal structure of a reference sample ZF-2 was created and is depicted in Figure 3(d). In figure 3(d), the $ZnFe_2O_4$ consists of 2 formula per unit cell with Zn at (0, 0, 0), Fe at (0.625, 0.625, 0.625) and O at (0.375, 0.375, 0.375). The value of the lattice parameter was found to be greater for ZF-2 and ZF-4 than for ZF-0. Because of the difference in bond length, the variation in lattice parameter can be associated with the bond length Zn/Mn-O (See Table 1). However, as Mn content increased, the bond angle O-Zn-O decreased. As Mn occupied the Zn-site, the bond angle rose, which could be attributed to the greater ionic radii of Mn^{2+} than Zn^{2+} , however it slightly dropped for sample ZF-4, which could be attributed to the presence of mixed valence

states of Mn^{2+}/Mn^{3+} . The presence of mixed valence state of Mn can be explained in terms of loss of oxygen, as shown by the following equation;



The presence of an electron in the preceding equation reduced the valence states of Fe, as shown by the following equation;



The presence of Fe^{2+} at Fe^{3+} causes an excess of negative charge ($Fe^{2+}_{Fe^{3+}}$) that can be compensated by the generation of hole (h^{\cdot}). The hole was captured by Mn^{2+} and oxidized to Mn^{3+} , which explains the difference in structural parameters [34]. In addition, the effect of Mn substitution at the Zn site has been studied in more detail in subsequent sections.

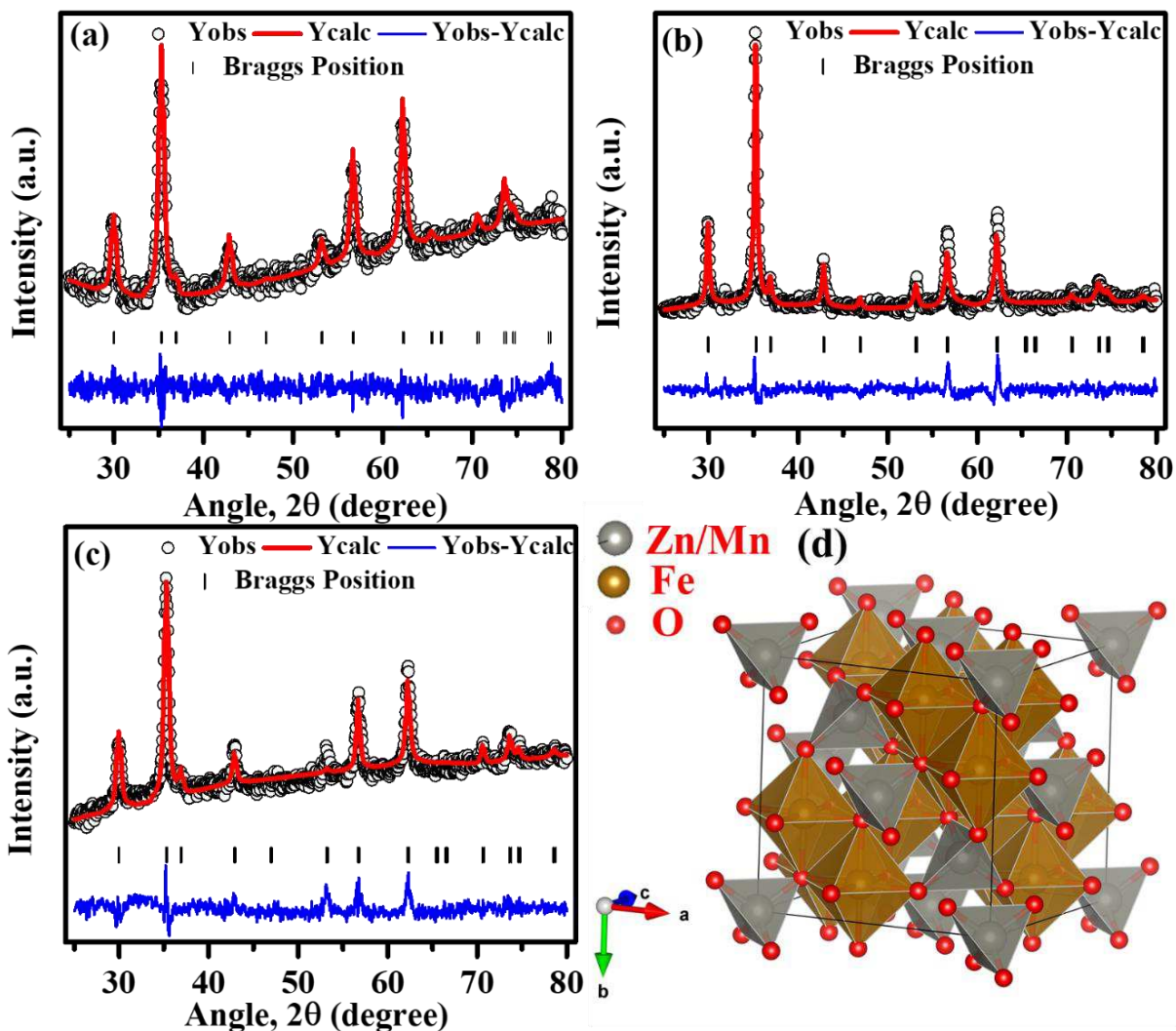


Figure 3: Rietveld refinement pattern of all samples generated using FullProf Software, (a) ZF-0, (b) ZF-2, (c) ZF-4, (d) A reference crystal structure of sample ZF-2 generated from refinement data.

Crystallite size and Micro-Strain analysis

The presence of many types of contributions, such as instrumental broadening, small crystallite size, micro-strain, wavelength selection, radiation filter, and so on, is reflected in the broadening of XRD peaks. Williamson and Hall devised a formula for calculating crystallite size and micro-strain from the full width half maxima (FWHM) of an XRD peak, popularly known as the W-H

plot. The crystallite size (D) and micro-strain (ε) were related to each other using the W-H plot, as shown below [35]:

$$\beta \cos\theta = \varepsilon \sin\theta + \frac{k\lambda}{D} \quad (3)$$

Where, β is FWHM of XRD peak, k is Scherrer constant, λ is the wavelength of Cu $K\alpha$ radiation, and θ is the angular position of each XRD peak. Figure 4 depicts the plots created for each sample using equation (3). A linear equation, $y = mx + c$; $y = \beta \cos\theta$, $x = \sin\theta$ has been fitted to the experimental data shown by a solid line in Figure 4. The intercept and slope of the linear equation were used to compute the crystallite size and micro-strain in the sample, and the results are shown in Table 1.

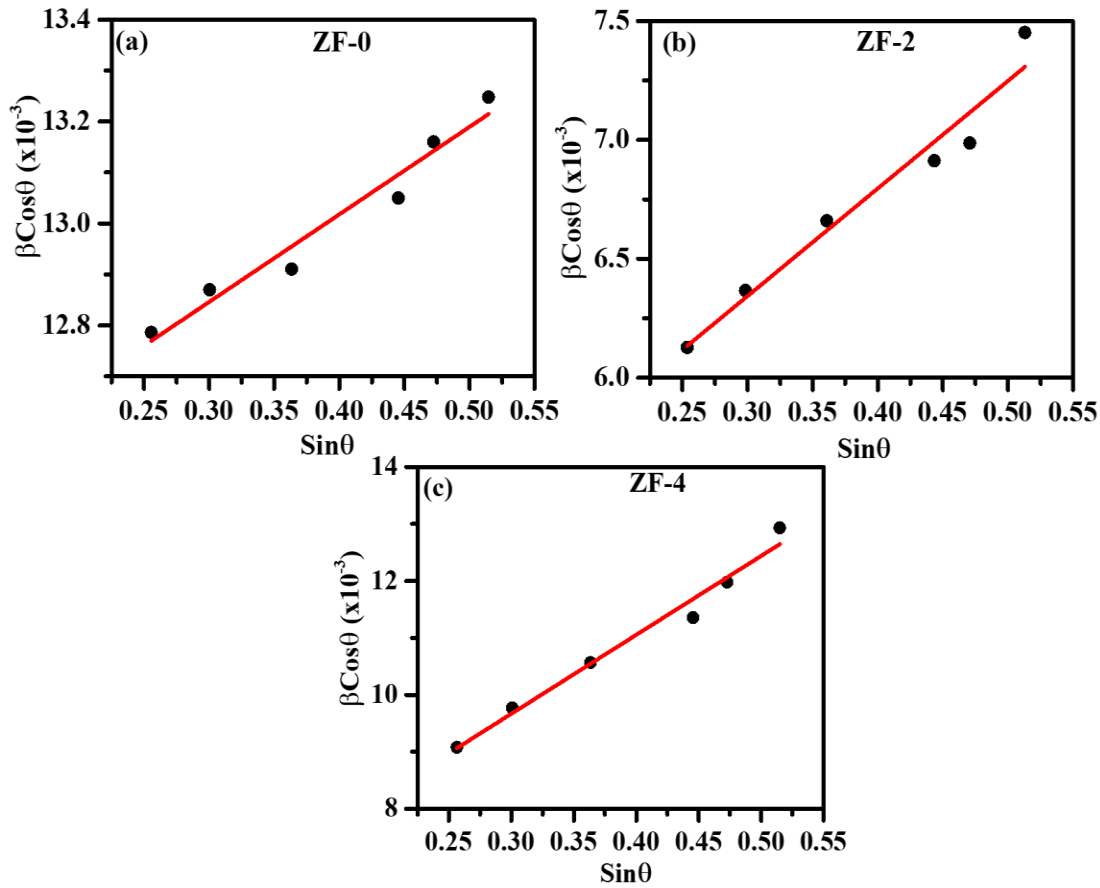


Figure 4: Williamson-Hall (W-H) plot generated using equation (3) for all samples (a) ZF-0, (b) ZF-2, (c) ZF-4.

Table 1: Structural parameters, Rietveld refinement parameters, atomic coordinate, occupancy, Crystallite size, micro-strain, and Zeta potential parameters of all samples.

Parameters	ZF-0	ZF-2	ZF-4
Crystal Structure	Cubic	Cubic	Cubic
Lattice angle (°)	$\alpha = \beta = \gamma = 90$	$\alpha = \beta = \gamma = 90$	$\alpha = \beta = \gamma = 90$
Lattice Parameter (a=b=c) (Å)	8.4340	8.4417	8.4372
Volume (Å ³)	599.93	601.58	600.61
Rietveld Refinement Parameters			
R_p	2.41	1.88	2.22
R_{wp}	3.04	2.62	2.90
R_{exp}	2.19	2.11	2.14
χ^2	1.91	1.54	1.83
$S = R_{wp}/R_p$	1.26	1.39	1.30
Zn/Mn-O (Å)	1.8078	1.8264	1.8142
Fe-O (Å)	2.0875	2.0888	2.0894
O-Zn-O (°)	108.64	109.47	108.92
O-Fe-O (°)	180.00	180.00	180.00
Atomic Coordinate			
Zn/Mn	(0,0,0)		
Fe	(0.625, 0.625, 0.625)		
O	(0.375, 0.375, 0.375)		
Occupancy			
Zn-8a	1.000	0.976	0.951
Mn-8a	0.000	0.019	0.038

Fe-16d	2.000	1.990	1.985
O-32e	3.992	3.972	3.984
Crystallite Size (nm)			
W-H plot	10.23	25.43	22.72
SSP plot	11.20	27.78	25.51
Micro-strain ($\times 10^{-3}$)			
W-H plot	1.72	4.52	13.84
SSP plot	5.00	6.05	11.10
Zeta Potential Measurement			
Zeta Potential (mV)	19.2	15.4	10.2
Hydrodynamic Size (nm)	130.0	590.1	277.3
PdI	0.968	0.971	0.613

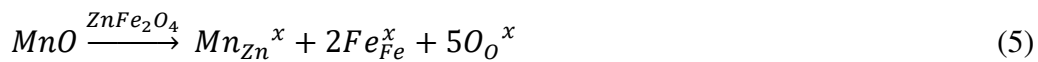
Table 1 shows that the crystallite size is larger for ZF-2 than for ZF-0, but slightly smaller for sample ZF-4 than for ZF-2. Crystallite size varies in the same way that structural characteristics such as lattice parameter and unit cell volume do (See Table 1). On the other hand, the value of micro-strain gradually increases with Mn doping concentration. A larger change in micro-strain seen for sample ZF-4 could indicate the presence of Mn^{3+} in the sample. Since in W-H plot, it largely focuses on the reflection obtained at the lower angle, where the error function is significant [36]. Thus, the value of crystallite size and micro-strain obtained from W-H plot is not reliable. As a result, researchers are attempting to develop a new method for properly assessing crystallite size and micro-strain. A new relation known as the "**Size-Strain plot (SSP)**" has been used for better determination of crystallite size and micro-strain of the samples [37].

Since the dopant Mn (Mn^{2+}/Mn^{3+}) at the Zn site can be homovalent or hetrovalent; so, the dopant contribution had a considerable impact on crystallite size and micro-strain. The lattice strain (defined as the ratio of gradual change of the lattice parameter to its initial value) induced within the samples causes the shift in interplanar spacing (d-spacing). The change in interplanar spacing is determined by the nature of the strain occurring between the planes (d). Compressive strain causes shift in angular position towards higher angle, whereas tensile strain causes a shift in angular position towards lower angle. The crystallite size and lattice strain developed in each sample have been estimated using the ‘Size–Strain Plot’ (SSP) represented by the equation;

$$\left(\frac{d_{hkl}\beta\cos\theta}{\lambda}\right)^2 = \frac{k\lambda}{D}\left(\frac{d_{hkl}^2\beta\cos\theta}{\lambda^2}\right) + \left(\frac{\varepsilon}{2}\right)^2 \quad (4)$$

Where, d_{hkl} is the interplanar spacing of particular (hkl) plane, and the other parameters used in equation (4) are already described in equation (3). The SSP plot for all samples generated using equation (4) are shown in Figure 5. A linear equation $y = mx + c$ has been fitted to the experimental data point by considering $y = \left(\frac{d_{hkl}\beta\cos\theta}{\lambda}\right)^2$ and $x = \left(\frac{d_{hkl}^2\beta\cos\theta}{\lambda^2}\right)$ that gives slope $m = \frac{k\lambda}{D}$ and intercept $c = \left(\frac{\varepsilon}{2}\right)^2$. The value of intercept has been used to calculate micro-strain, whilst the value of the slope has been used to calculate crystallite size of all samples. The value of crystallite size and micro-strain for all samples were given in Table 1.

Crystallite size obtained from W-H plot and SSP plot show similar trend of variation with Mn doping in $ZnFe_2O_4$. However, the value of micro-strain is again found to increase with doping of Mn in $ZnFe_2O_4$. As previously stated, Mn acts as both a hetrovalent and a homovalent type substitution, and the charge compensation mechanism occurs in the system in the following manner:



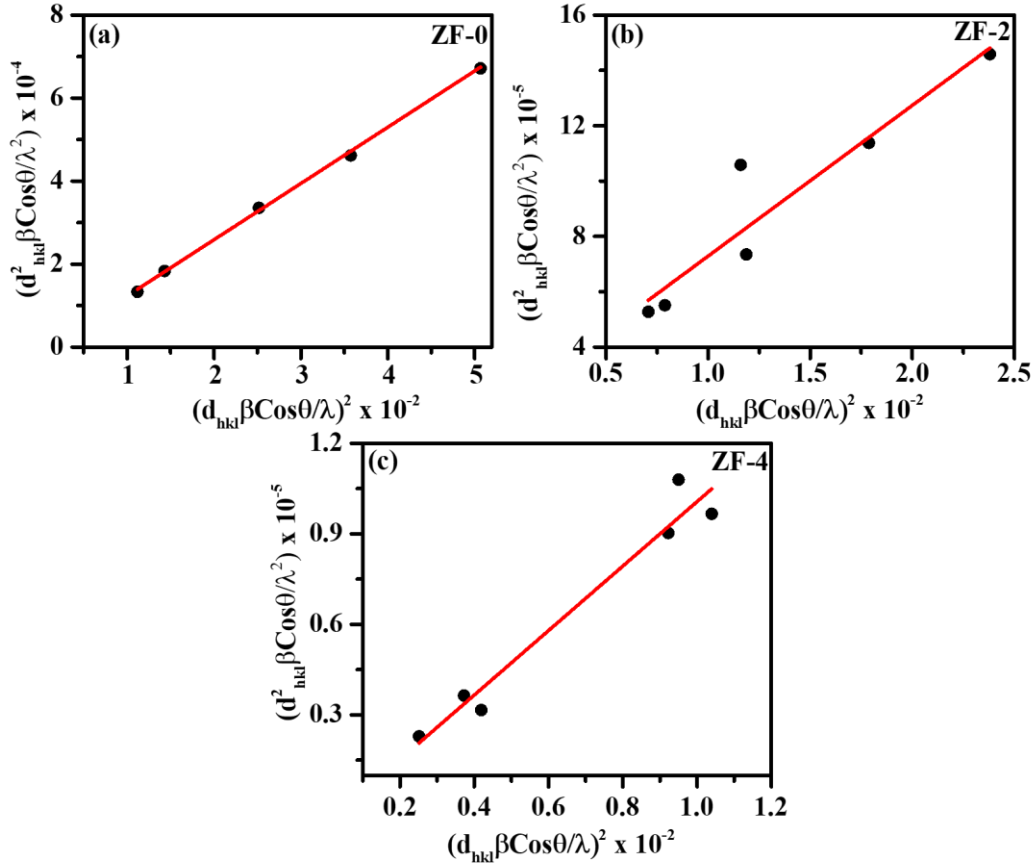
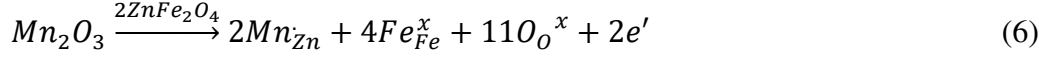


Figure 5: Size-Strain Plot (SSP) generated from XRD data using equation (2) for all samples, (a) ZF-0, (b) ZF-2, (c) ZF-4.

Since the ionic radii and the defects of samples play a crucial role in the growth of crystallization [36], so higher crystallite size observed in the case of ZF-2 compared to ZF-0 might be due to higher ionic radii of Mn (See equation (5)). The increase in doping concentration of Mn leads to charge compensation processes partially as per equation (5) and (6), due to presence of Mn in mixed valence state ($\text{Mn}^{2+}/\text{Mn}^{3+}$) (as described in Rietveld refinement analysis). The donor type substitution acts as grain growth inhibitor [38]; that might be possible reason for decrease in the crystallite size of sample ZF-4. Moreover, gradual increase of micro-strain may be associated to

the difference of ionic radii between Mn and Zn, as well as the existence of defects as shown by equation (5) and (6) (See Table 1).

Zeta potential analysis:

The zeta potential is the potential difference between the surface of a solid immersed in a conducting liquid and the bulk of the liquid (ζ) [39]. Nanoparticles appear to have a surface charge, which attracts ions of opposite charges to the surface. The electro-kinetic potential of undoped and doped ZF samples was calculated by dispersing a pinch of powder into water solutions. Figure 6 depicts the Zeta potential curve for all samples, and Table 1 lists their numerical values. To see the effect of Mn, the peak with the highest intensity was taken into account. The zeta potential for sample ZF-0 is found to be +19.2 mV, and it decreases with Mn doping to 15.4 mV and 10.2 mV for samples ZF-2 and ZF-4, respectively, indicating the presence of a negative defect on the surface of the samples (See equation 6). With careful observation, it was noticed that sample ZF-2 has a weak intensity peak towards negative potential vanishes in sample ZF-4; this observation also reflects the presence of Mn in varying valence states.

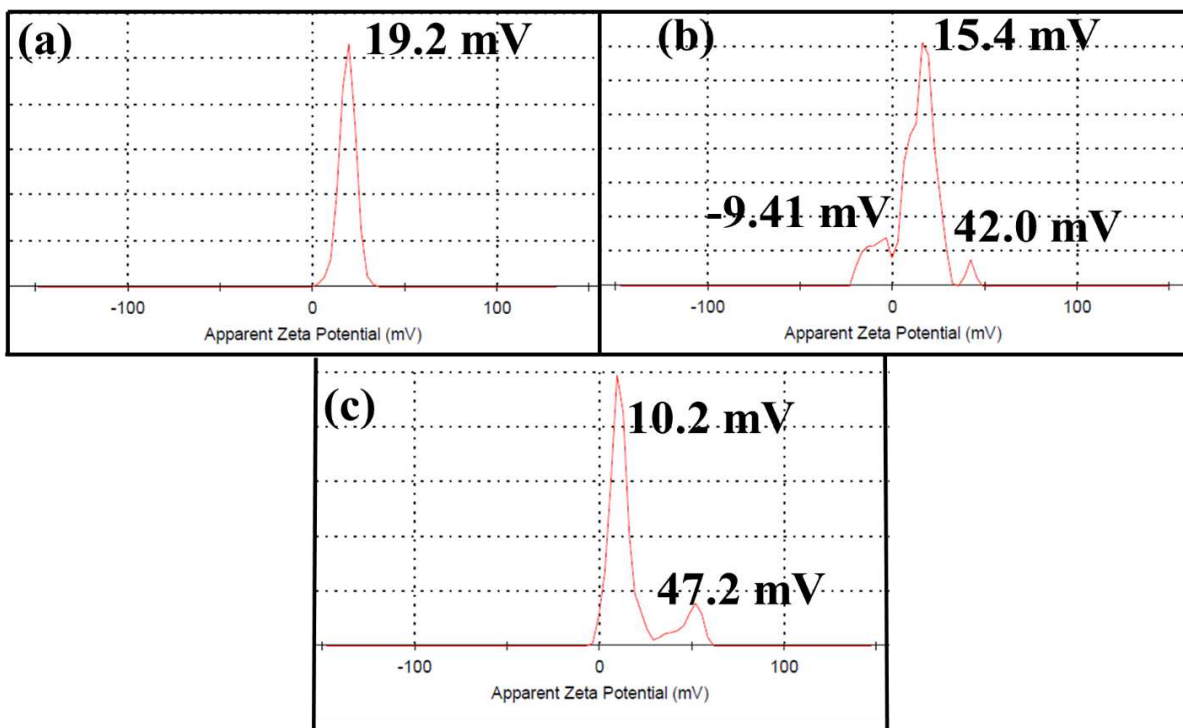


Figure 6: Zeta potential curve of samples, (a) ZF-0 (b) ZF-2 (c) ZF-4.

In addition, all samples' hydrodynamic size and polydispersity index (PdI) were determined by measuring zeta potential using the dynamic light scattering (DLS) mechanism, as shown in Figure 7. Table 1 lists the numerical values of hydrodynamic size and PdI for all samples. For various colloidal structures, there is a pH value at which the electrokinetic potential is equal to zero, and this point is known as an iso-electric point. Furthermore, colloidal coagulation is not overwhelmed by electrostatic repulsion [6]. It is a well-known phenomenon that the value of zeta potential ± 30 mV is thought to be the limit value for determining the stability of the dispersion in the water system. In this case, the zeta potential is less than 30 mV, ensuring that electrostatic attraction remains stable during the dispersion of ferrites nanopowder [40]. The largest dimension of the spherical particle is defined by the hydrodynamic diameter of the sample [41]. Table 1 shows the average width of the spherical particle obtained using this method. The hydrodynamic size of the samples follows a similar trend with Mn as observed for crystallite

size. On the other hand, the magnitude of hydrodynamic dimension is much larger than the crystallite size, implying that a single particle is made up of several crystallites. However, PdI greater than 0.5 indicates that the nanopowder remain stable under the DLS mechanism [6, 41].

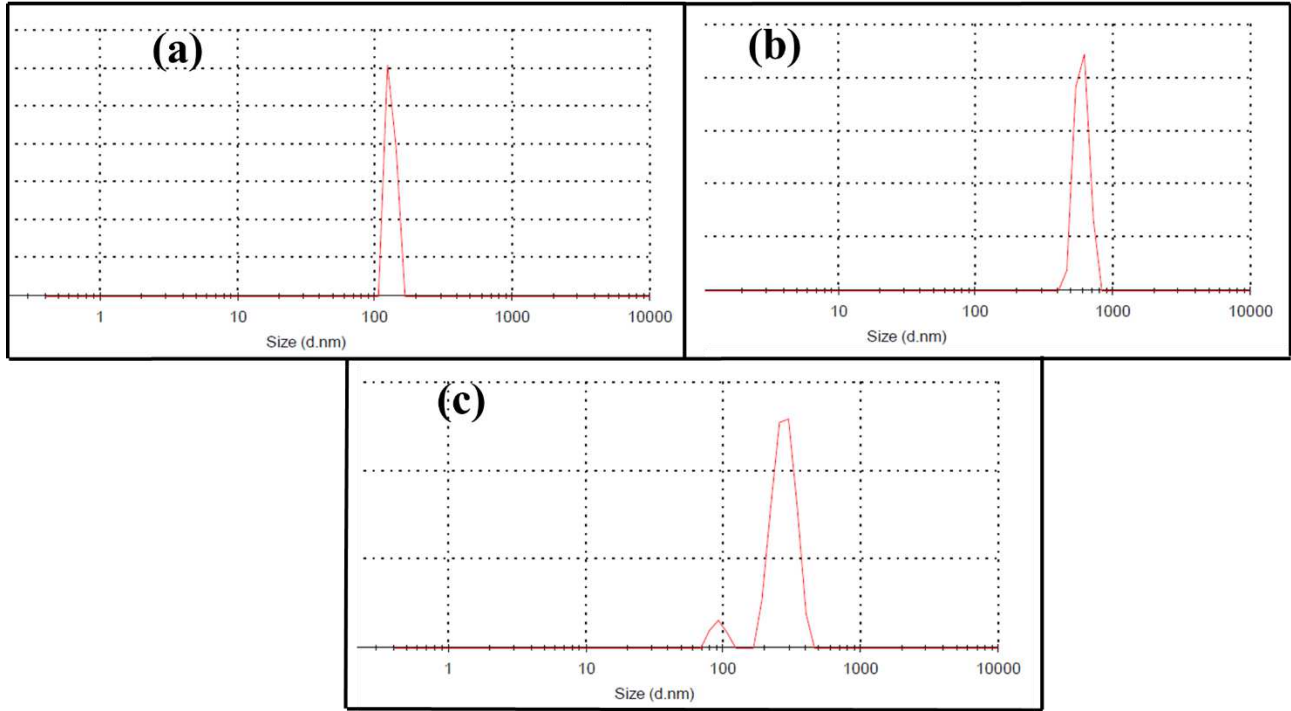


Figure 7: Hydrodynamic size distribution curve of all samples under DLS scheme, (a) ZF-0 (b) ZF-2 (c) ZF-4.

Raman Spectra analysis

Figure 8 depicts the Raman spectra of prepared samples as a function of the position of the Raman bands and their intensity. $ZnFe_2O_4$ crystallizes into a cubic spinel group under $Fd\bar{3}m$ space group by eight formula units such that $8x(ZnFe_2O_4)=56$ atoms [42]. In this complete spinel group the distribution of metallic cation can be written in terms of $(M_{1-x}Fe_x)^{2+}$ shared by tetrahedral sites while $(Fe_{2-x}M_x)^{3+}$ shared by octahedral sites, where M can be Zn/Mn in present case. The group theory investigation of the $ZnFe_2O_4$ spinel structure yielded 42 modes, three of which were acoustic and 39 of which were optical [6].

$$\Gamma_{total} = A_{1g}(R) + E_g(R) + 3F_{2g}(R) + 2A_{2u} + 2E_u + 4F_{1u}(IR) + 2F_{2u} \quad (7)$$

Where, R denotes Raman active modes and IR denotes infrared active modes while other modes are found to be inactive or silent. The terms “A” and “E” represent 1-dimensional and 2-dimensional vibrations while the subscript “g” and “u” denotes symmetry and anti-symmetry vibrational modes respectively [43]. Out of the 42 modes as mentioned above, only five modes are found to be Raman active such that $A_{1g} + E_g + 3F_{2g}$. The position of these bands was recorded from Figure 8 and given in Table 2. The vibrational band A_{1g} is associated with Zn/Mn-O vibration that originates at tetrahedral site, while $F_{2g}(1)$, E_g , $F_{2g}(2)$, and $F_{2g}(3)$ are attributed to the vibration of Fe-O at octahedral sites. On careful observation, it has been further noticed that the vibrational band observed at 657 cm^{-1} for sample ZF-0, shifts towards the lower wavenumber for ZF-2 and ZF-4. The vibrational frequency of the particular band is inversely proportional to the moment of inertia ($I = \mu r^2$), where μ is reduced mass and r is lattice constant. Since the vibrational frequency depends on reduced mass and lattice constant that plays a crucial role and affect the position of Raman active bands. Since, the atomic mass of Mn (54.94 A.U.) is smaller than the atomic mass of host Zn (65.38 A.U) [44]. The lattice constant for ZF-2 sample was found to be higher, resulting in a shift of the position of the Raman band towards the lower side than ZF-0, whereas the lattice constant for ZF-4 sample was found to be slightly lower than ZF-2, resulting in a shift of Raman bands towards the higher wavenumber.

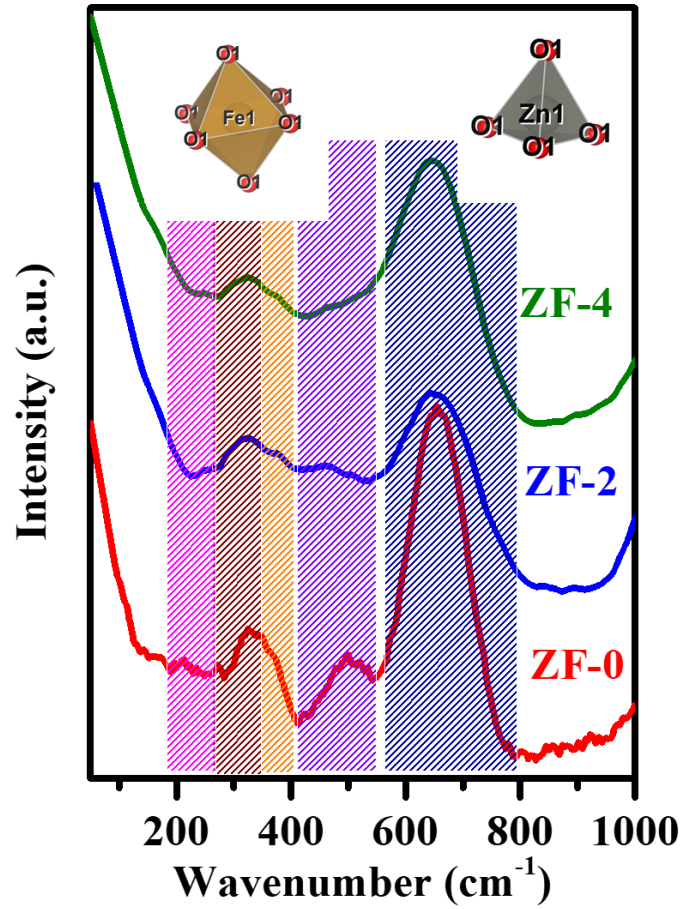


Figure 8: Raman spectrum of all samples recorded at room temperature.

Table 2: Position of Raman band observed in all samples, and their vibrational mode

Vibrational Band	Position of Raman Band (cm^{-1})		
	ZF-0	ZF-2	ZF-4
$F_{2g}(1)$	211	243	251
E_g	274	320	331
$F_{2g}(2)$	337	377	380
$F_{2g}(3)$	497	471	466
A_{1g}	657	635	644

Ultraviolet-Visible (UV-Vis.) spectroscopy analysis:

The optical bandgap of prepared samples was determined using UV-Vis. Spectroscopy with the help of well-known relation known as Tauc equation. According to Tauc, the absorption (α) of a material is related to its optical bandgap (E_g) by the following relation [45]:

$$(\alpha hv)^2 = B(hv - E_g) \quad (8)$$

Where, B is a temperature independent constant, hv is the energy of the incident photon. The optical bandgap of a material is defined as the separation between the valence band to conduction band. Therefore, in order to determine the value of optical band gap, the plot between $(\alpha hv)^2$ and hv has been generated for all samples and shown in Figure 9. On careful observing the equation (8), the nature of variation is straight line $y = mx + c$; with $y = (\alpha hv)^2, c = E_g$. The linear portion of the plot has been extrapolated on the X-axis at $(\alpha hv)^2 = 0$, that gives the value of optical bandgap and mentioned in each figure. The optical bandgap of undoped $ZnFe_2O_4$ has already been published in the literature, i.e., 2.27 eV, which is smaller than the optical bandgap of obtained $ZnFe_2O_4$ in this study. The difference in optical bandgap could be attributed to the smaller crystallite size of sample [46]. However, with incorporation of Mn the bandgap was increased to 2.51 eV for ZF-2 and reduced to 2.13 eV for ZF-4. The optical bandgap in $ZnFe_2O_4$ is the result of a transition from 3d orbital of Fe^{3+} to the 2p orbital of O^{2-} . The variation observed in Table 1 for band gap followed the similar trend as seen for the crystallite size. Many scientific reports suggest that the direct bandgap is inversely proportional to the crystallite size, that contradicts our present result [47]. Although the similar types of variation are already reported in the literature [35, 48, 49].

Kumar et al. studied the influence of Ti^{4+} on the optical bandgap of $CaSnO_3$ and how it relates to lattice strain. They reported that with incorporation of Ti^{4+} at Sn^{4+} site of $CaSnO_3$ leads decrease

of crystallite size as well as increase of lattice strain. They also reported that the optical bandgap decreases with decreasing the crystallite size [35]. Nair et al. also stated that increasing lattice strain for extremely small size particle raises the surface pressure, which increases the direct optical band gap. From both papers, three factors may influence the bandgap of nanomaterials [49];

- (i) Interfacial or Surface effect
- (ii) Variation in crystal structure by heat treatment
- (iii) Presence of Lattice strain in sample.

In the current sample, factors I and (iii) were used. Table 1 demonstrated that the micro-strain increases with increasing doping concentration and accurately matches the optical bandgap change seen in the current study. The presence of defects such as e' , h' , and Mn_{Zn} are already described in ZF-4 sample during structural analysis. As doping concentration increases, there is a possibility of overlapping between the conduction band and the defect energy level, resulting in a reduction of the optical bandgap [37, 50]. The representation of the defect level, valence band and conduction band in energy level diagram is shown in Figure 9 (d).

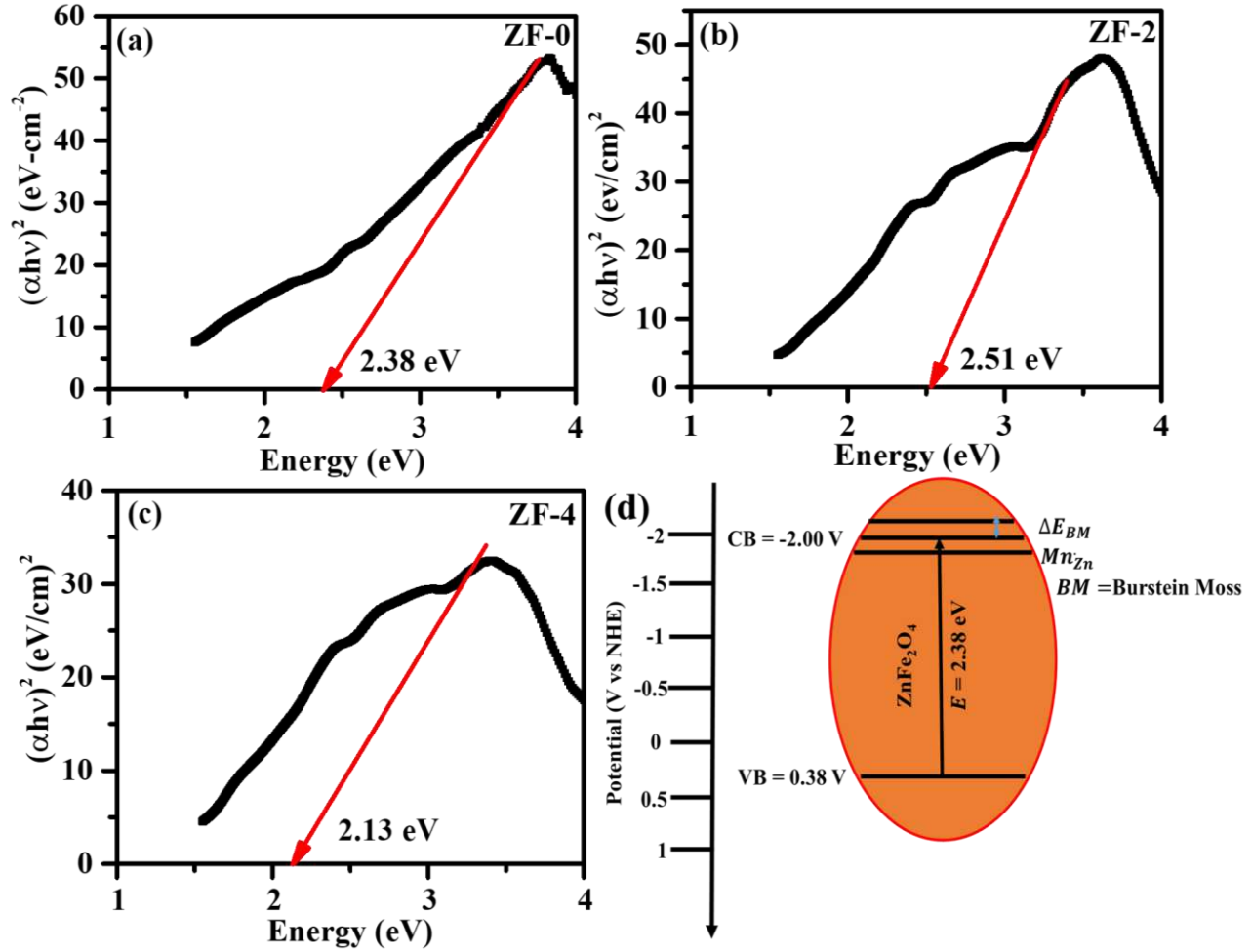


Figure 9: Tauc plot generated for all samples using equation (8). (a) ZF-0, (b) ZF-2, (c) ZF-4 Black line shows experimental data while red line shows the fitted data. (d) Energy Band Diagram.

Characterization of sintered pellets:

Microstructural analysis using Scanning Electron Microscope (SEM):

The microstructural properties of all prepared powders and sintered pellets were recorded and shown in Figure 10. All the images of samples were recorded at same magnification of $2 \mu\text{m}$. Figure 10 (a-c) depicts the microstructure of prepared powder sample, that significantly shows the distribution in the size of grains ranging in the range of $(0.10\text{-}0.17) \mu\text{m}$, $(0.09\text{-}0.14) \mu\text{m}$ and $(0.10\text{-}0.14) \mu\text{m}$ for sample ZF-0, ZF-2 and ZF-4 respectively. The particles in the samples were

observed to be highly agglomerated, with many pores. The doping of Mn at the Zn-site steadily increases the number of grain boundaries and pores which decreases the grain size. Furthermore, as seen in Figure 10 (d-f), the microstructure of the samples altered dramatically during sintering of the pellets. With sintering, particle aggregation and grain boundaries were minimized. The microstructure of the samples was spherical in shape, resembling the cubical structure of ferrites. When the microstructures of powder and sintered samples were compared, it was discovered that the microstructures of all samples became denser for sample ZF-0, lowest for sample ZF-4, and intermediate for sample ZF-2.

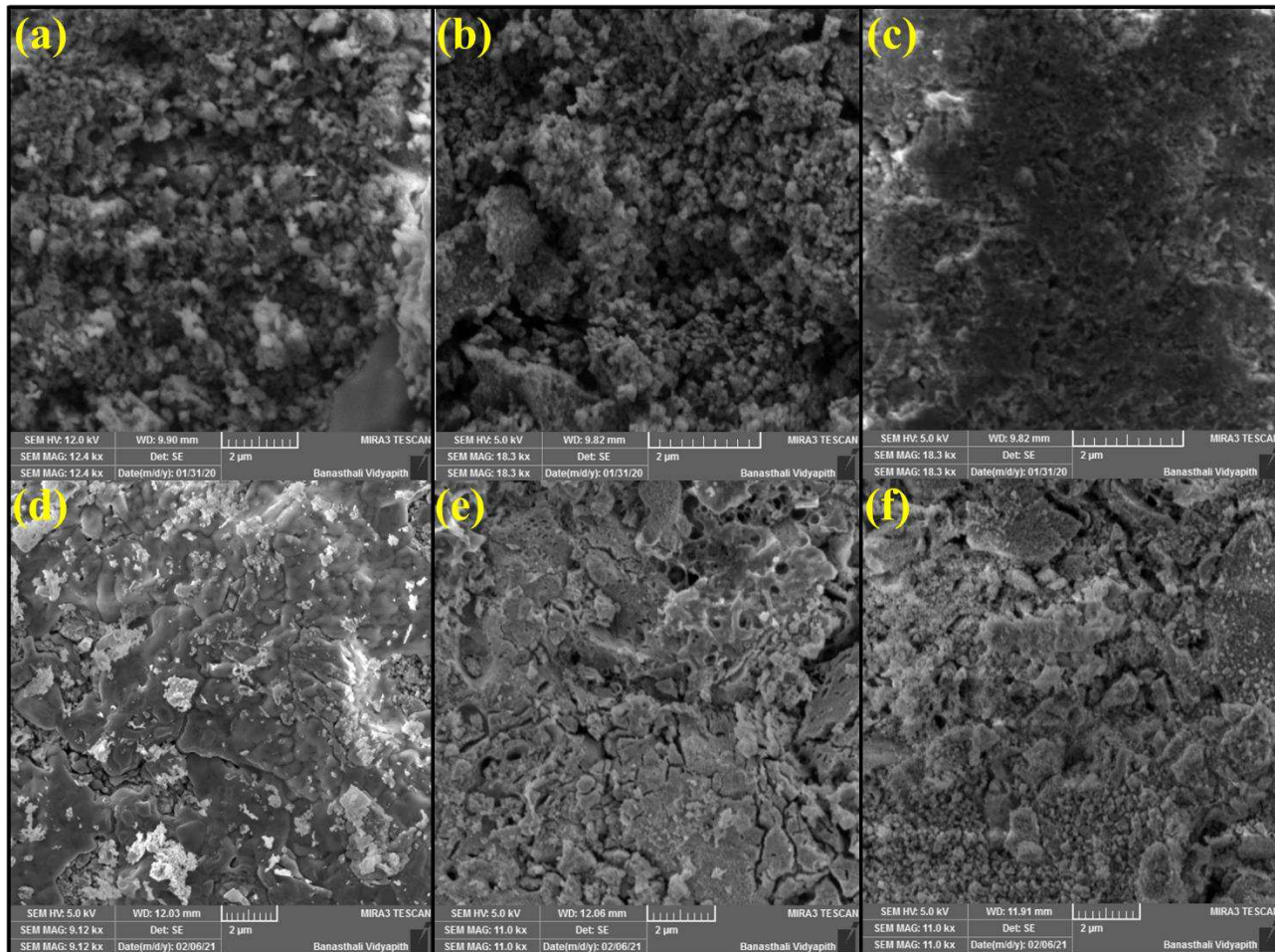


Figure 10: Scanning electron micrograph (SEM) of (a-c) prepared powders and (d-f) sintered pellets of $Zn_{1-x}Mn_xFe_2O_4$ (a, d) ZF-0, (b, e) ZF-2, (c, f) ZF-4.

The grain size of the samples was taken into account in order to explore the influence of Mn on the microstructural properties. Figure 11 depicts a histogram of the number of grains and their sizes generated with the “**ImageJ**” software. The average grain size of samples was determined by fitting of Gaussian function to the histogram. Mn doping was shown to reduce the average grain size of samples. Since XRD and UV-Vis studies indicated the existence of Mn in Mn^{2+}/Mn^{3+} states in the samples, and the charge compensation mechanism was takes place by equation (5) and (6). The existence of defects played an important part in the grain growth process, which can be explained by the following explanations;

- (i) In the case of homovalent substitution, the difference in the ionic radii of the host and dopant caused lattice strain, which increased the surface and interfacial defect considerably. The columbic strength (either repulsive or attracting) between two adjoining grain atoms increases as they get closer. It is well known that grain boundaries are more disordered than grain; if both grains have opposite charges, it attracts and results in larger grain size, which is known as grain growth promoter; if both grains have the same charge, it repels and results in smaller grain size or formation of a void among the grains, which is known as grain growth inhibitor [51].
- (ii) In case of hetrovalent substitution, there is difference in the charge either in terms of oxygen vacancies or cationic vacancies. The presence of these defects controlled the microstructure of samples as discussed in reason (i). The literature suggests that the donor acts as grain growth inhibitor while acceptor acts as grain growth promoter [52].

In this situation, both explanations are used to explain the microstructural variation. In sample ZF-2, the lattice strain increases, causing the surface pressure to rise and the grain size to shrink.

In the instance of ZF-4, however, the substitution is partially homovalent and partially donor type; thus the grain size reduced.

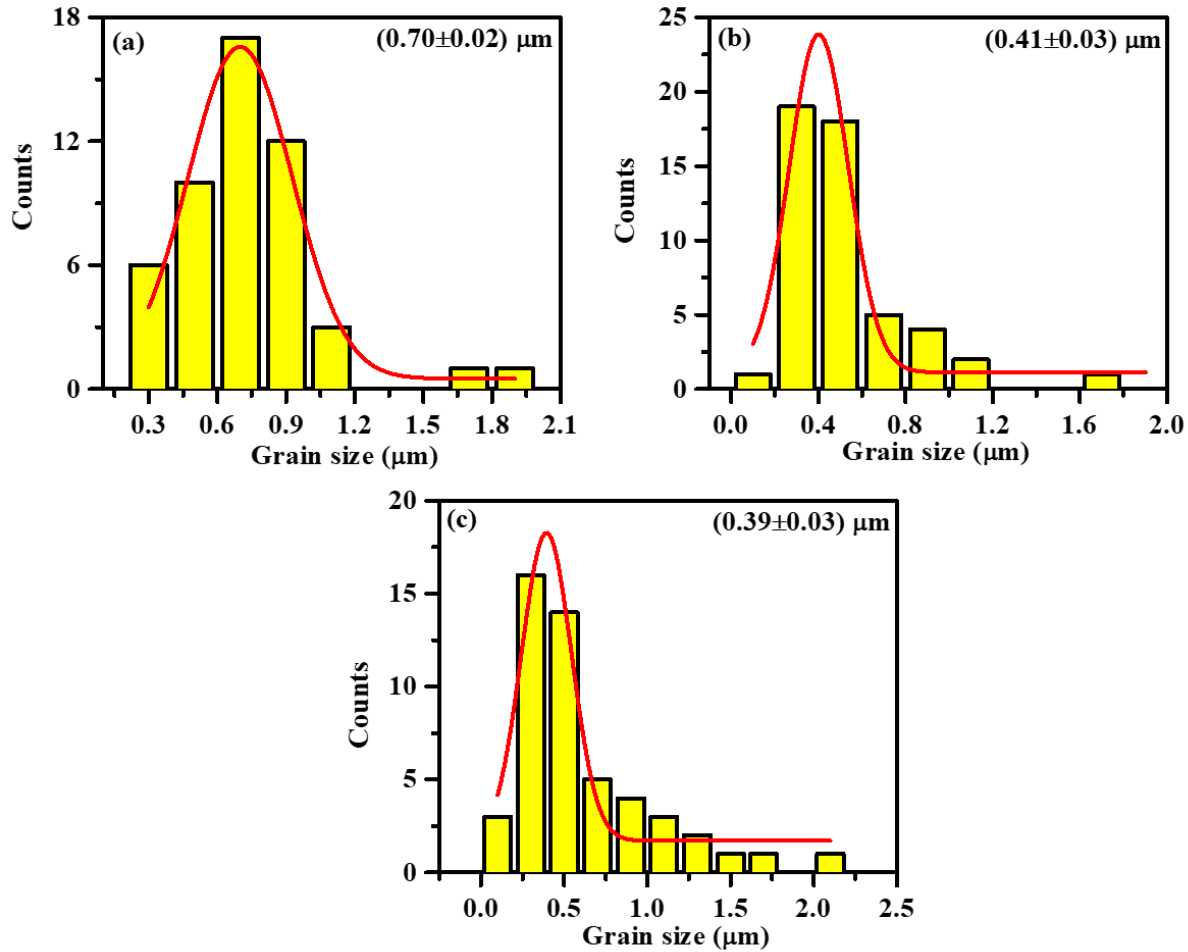


Figure 10: Histogram between the No. of grains and grain size of Zn_{1-x}Mn_xFe₂O₄ samples (a) ZF-0, (b) ZF-2, (c) ZF-4.

Dielectric and Dissipation factor study of sintered pellets:

The dielectric properties of sintered pellets were studied as a function of temperature (50-600) °C at various frequencies such as 1 KHz, 10 KHz, 100 KHz, and 1 MHz. Figure 11 (a, c, e) and 11 (b, d, f) illustrate the variation of dielectric constant (ϵ) and dissipation factor (D) with temperature at different frequencies for samples ZF-0, ZF-2 and ZF-4 respectively. The dielectric constant and dissipation factor of all samples have increased with temperature and decreased

with frequency. The variation in dielectric constant and dissipation factor was well explained by Koop's theory. According to this theory, the dielectric constant decreased with frequency can be represented by assuming the solid as composed of conductive grains separated by bad conducting grain boundaries that takes more time to respond in the presence of smaller a.c. field. As a result, at lower frequencies, the dielectric constant is larger, while at higher frequencies, the dielectric constant is lower [53].

Since the dielectric properties of oxides, ferrites, perovskite, and ceramics are governed by four types of polarizations: interfacial polarization, orientational polarization, ionic polarization and electronic polarizations [54]. These polarizations are active within a certain frequency range. All types of polarizations were found to be operative in between 1 mHz to 1 KHz, and as frequency increased, the polarizations were eliminated one by one. Interfacial polarization was ruled out above 1 KHz, orientational polarization was ruled out above 1 MHz, and ionic polarization was ruled out above 1 GHz. As a result, only interfacial and orientational polarization have been found to be active in samples within the studied frequency range. The dielectric constant and dissipation factor of sample ZF-0 exhibit two peaks at 1 KHz, and single peak at 100 KHz and 1 MHz. Both peaks are found to be nearly equidistant in both plots, such as 432 °C and 560 °C at 1 KHz and 450 °C, in dielectric plot while at 400 °C and 452 °C at 100 KHz and 1 MHz respectively. However, only a single peak is found for sample ZF-2 at 400 °C, 350 °C, 455 °C in dielectric constant and 350 °C, 300 °C, 450 °C at 1 KHz, 100 KHz and 1 MHz respectively. Further, two peaks were found in dielectric and dissipation factor plots of sample ZF-4 at 450 °C and 550 °C in dielectric plot, and at 350 °C and 450 °C at 1 KHz while single peak at 400 °C and 400 °C in dielectric plot and 400 °C and 350 °C in dissipation factor at 100 KHz and 1 MHz respectively. Each reaction peak present in each curve reflects the mobility of different charge

carriers in the sample on application of smaller a.c. field on pellets [55]. Further, it has been noticed that the dielectric constant and dissipation factor were found to be stable up to 300 °C that makes it a suitable candidate for thermally stable capacitor application.

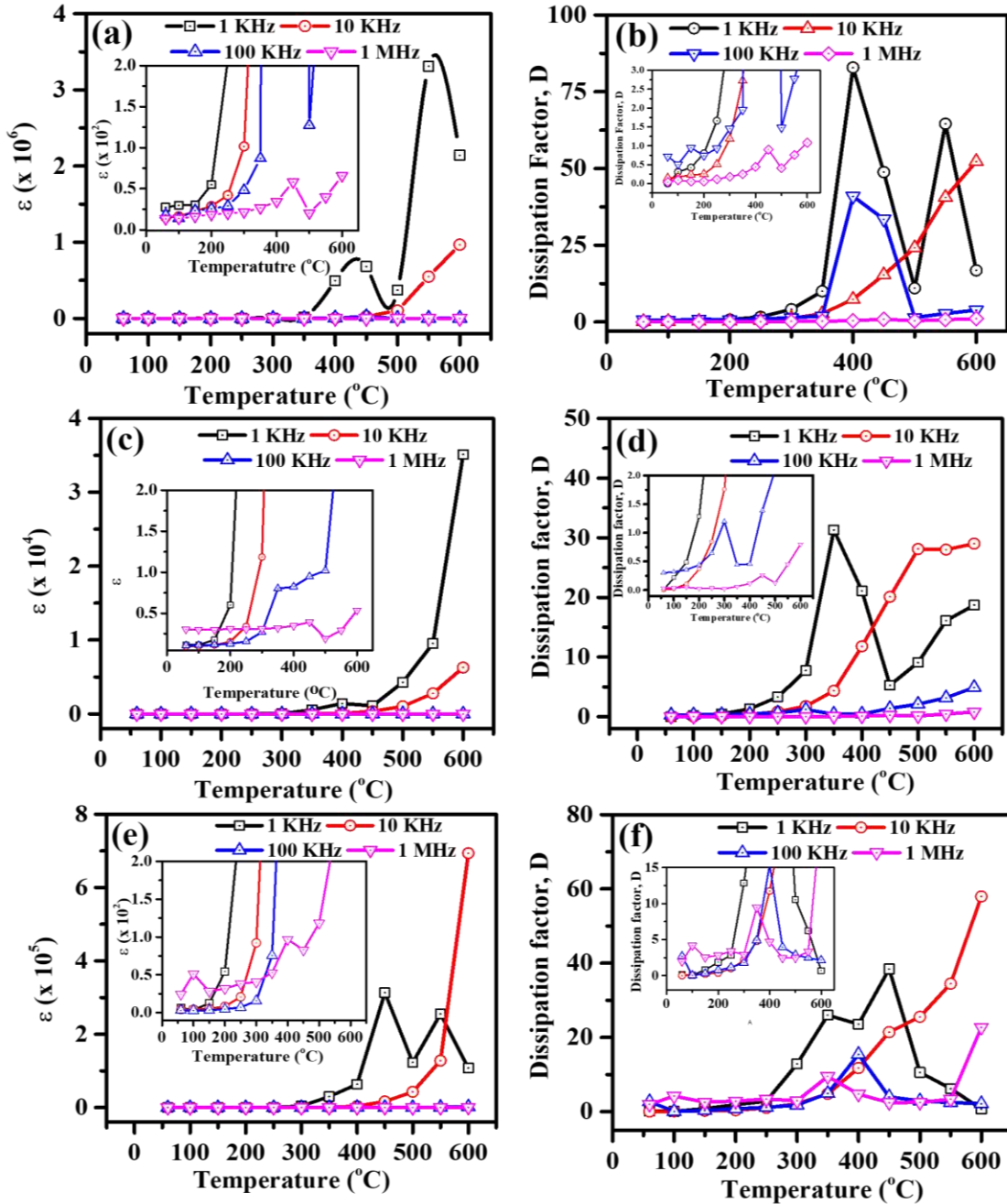


Figure 11: Variation of dielectric constant (ϵ) and dissipation factor (D) with temperature at different frequencies of sample (a-b) ZF-0, (c-d) ZF-2, (e-f) ZF-4 respectively.

Figure 12 (a) and (b) show the effect of Mn doping on dielectric constant and dissipation factor as a function of temperature at a constant frequency of 10 KHz. The dielectric constant of the undoped sample found to be higher, lowest for ZF-2 and in middle for ZF-4. The presence of oxygen vacancy and other defects in the samples are already described in structural analysis section.

In case of undoped sample (ZF-0), there are two types of defects present: oxygen vacancies ($V_o^{\cdot\cdot}$) (Eq. (1)) as positive charge, and the presence of Fe^{2+} at Fe^{3+} act as negative defect (Eq. (2)) denoted by $Fe^{2+}_{Fe^{3+}}$. The presence of these two defects away from each other results in the formation of a dipole ($V_o^{\cdot\cdot} - 2Fe^{2+}_{Fe^{3+}}$) and responds in the presence of a.c. field, resulting in dielectric constant as well as dissipation factor. Since the dielectric constant is proportional to the number of dipoles, and doping of Mn at the Zn site results a drop in the dielectric constant. This could be attributed to a decrease in number of dipoles. Furthermore, increasing Mn results in a small rise in dielectric constant over ZF-2. The compositional dependence of the dielectric constant and dissipation factor can be explained as follows:

- (i) Since Mn exist in Mn^{2+} in the case of ZF-2 (see structural analysis) and substitution of Mn^{2+} at Zn^{2+} leads neutral charge (equation (5)), which can be compensated by generation of micro-strain (see Table 1). The micro-strain may reduce the surface defects and chemical heterogeneity in the sample. Due to decrease in surface defect it further reduced the number of dipole, resulting drop in dielectric constant [54]. However, further increasing concentration of Mn leads to charge compensation mechanism by equation (5) and (6). Eq. (5) and (6) suggest presence of an extra defect $Mn^{3+}_{Zn^{2+}}$. The presence of defect $Mn^{3+}_{Zn^{2+}}$ increases the number of dipoles

such as $(V_o - 2Fe^{2+}_{Fe^{3+}})$ and $(2Mn^{3+}_{Zn^{2+}} - 2Fe^{2+}_{Fe^{3+}})$ that resulting rise in dielectric constant.

- (ii) The value of micro-strain increases with Mn doping, as shown in Table 1. As previously described in the XRD section, Mn doping results in a higher value of lattice parameter for ZF-2 sample and a minor rise over ZF-2 for ZF-4 sample. Since the separation between positive and negative charge is proportional to the lattice constant. When an a.c. field is applied, the dipoles respond by either jumping of electrons or orientation of dipole, resulting in a higher value of dielectric constant. However, if the separation is large enough, neither dipoles nor charge occurs, resulting in a decrease of dielectric constant. So, if the change in lattice constant is larger, the dielectric constant is smaller, and vice versa [36].

Since the change in dissipation factor appears to be similar to the variation in dielectric constant, therefore both the reasons discussed above may be appropriate to explain the variation seen in Figure 12 (b). The comparison between the present result with literature has been summarized in Table 3. The comparison clearly reveals that the current materials have a greater dielectric constant and a lower dissipation factor. Furthermore, the dielectric constant and dissipation factor are found to be stable up to 300°C, making it a good option for thermally stable capacitor and barrier layer capacitor applications. Above 300 °C, however, the variation is found to be linear, making it a suitable choice for gas sensors functioning on capacitive behavior applications.

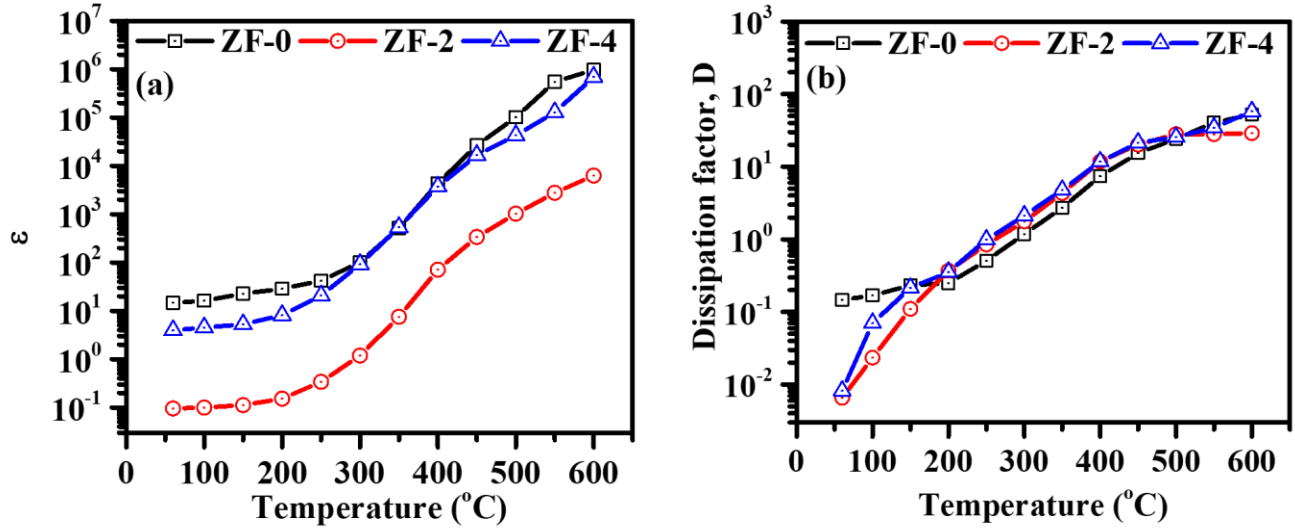


Figure 12: Variation of (a) Dielectric constant (b) Dissipation factor, with respect to temperature at 10 KHz frequency.

Table 3: Comparison of dielectric constant, dissipation factor, and conductivity of Zn_{1-x}Mn_xFe₂O₄ obtained in present work with those reported in the literature.

Composition	Synthesis route	Dielectric constant (ϵ)	Dissipation factor (D)	Conductivity (σ) [S-cm ⁻¹]	Reference
ZnFe ₂ O ₄	Solvothermal	5-10	1-5	10 ⁻⁵ -10 ⁻⁴	[43]
ZnFe ₂ O ₄ :Er ³⁺	Coprecipitation	2-20	0.1-0.6	--	[56]
ZnFe ₂ O ₄	Solid State Reaction	10-100	1-10	10 ⁻⁷ -10 ⁻⁶	[57]
Ni _{0.5} Zn _{0.5} Fe ₂ O ₄	Mechanical Alloying	200-3000	0.1-100	--	[58]
ZnFe ₂ O ₄	Thin Film	9.8-11.4	0.1-1	10 ⁻⁹ -10 ⁻⁴	[59]
Zn _{1-x} Mn _x Fe ₂ O ₄	Sol-gel chemical route	0.1-10 ⁶	0.01-90	5.3x10 ⁻⁴ - 8.12x10 ⁻³	Present Work

DC conductivity analysis:

The thermal transport properties of all sintered samples were studied within the investigated temperature range by recording its dc conductivity. Here, the conductivity has not been calculated directly. Although it has been calculated from the resistance of sample. The d.c. conductivity (σ) relates with the resistance (R) by the formula; $\sigma = \frac{l}{RA}$, where l is the thickness of the pellets and A is the cross-sectional area of the pellets. The d.c. conductivity of all samples were calculated as a function of temperature and shown in Figure 13. According to Arrhenius equation, the correlation between σ and the temperature is as follows [60]:

$$\sigma = \sigma_0 \exp \left[\left(\frac{-E}{1000 * k} \right) * \left(\frac{1000}{T} \right) \right] \quad (9)$$

Taking the log of equation (9) on both sides it gives;

$$\log \sigma = \log \sigma_0 + \left(\frac{-E}{1000 * k} \right) * \left(\frac{1000}{T} \right) \quad (10)$$

Where, σ_0 is a constant, E is the activation energy for the conduction of the charge carrier, and k is Boltzmann's constant. The d.c. conductivity (σ) of sample increases with temperature, indicating that the samples are semiconducting. The optical band gap of samples determined from UV-Vis. analysis also supports the present result. The plot of d.c. conductivity as inverse of temperature of all samples show a straight line with a single conduction region within the investigated temperature range for sample ZF-0, two regions of conduction for sample ZF-2, and three regions of conduction for sample ZF-4. The value of activation energy was calculated by fitting the equation (10) to the experimental data and given in table 3. The activation energy obtained for all of the samples was substantially lower than half of their bandgap, ruling out direct conduction in the sample. However, the value of activation energy shows that conduction in the samples occurred due to defects present the samples. Based on the results of the aforesaid study, it was found that the sample contains various types of defects such as $V_o^{\bullet\bullet}$ and e' in the

sample, which controlled not only optical properties but also the electrical properties. The expression of total conductivity of Mn-modified ZF samples is given by:

$$\sigma_{total} = \sigma_i + \sigma_p + \sigma_n = 2e[V_o^{\cdot\cdot}]\mu_{V_o} + ep\mu_p + en\mu_e \quad (11)$$

Where, σ_i is the conductivity of ion, σ_p is the conductivity of hole, and σ_n is the conductivity of electrons and μ represents mobility and its subscript specify the type of charge. The activation energy of sample ZF-0 was determined to be 0.87 eV, which falls within the range of activation energy predicted for the migration of doubly- ionized oxygen vacancies ($V_o^{\cdot\cdot}$) in perovskite oxides [61]. According to equation (11), total conductivity is affected not only on charge carrier concentration but also on the mobility of distinct charge carriers. In addition to oxygen vacancy, the contribution of other factors is not zero, although it is minimal. The typical value of activation energy for the conduction of $V_o^{\cdot\cdot}$ was found to be in the range of 0.55–1.30 eV [32]. However, in the case of sample ZF-2, two regions of conduction assigned as R-1 and R-2, were active within the investigated temperature range with activation energies of 0.45 eV and 0.74 eV respectively. The activation energy of R-2 was found to be higher than that of R-1, and the charge carriers present in the sample for the conduction are either oxygen vacancies or electrons. Since the value of activation energy was found to be lower than ZF-0, this could be owing to the association between the dipole defect viz; $V_o^{\cdot\cdot} - 2Fe^{2+}_{Fe^{3+}}$. Strong association between these two defects needs a higher activation energy for migration, and breaks after certain temperature. As a result, it requires less activation energy to move across the lattice. Furthermore, for sample ZF-4, three conduction regions were identified as R-1, R-2, and R-3, with activation energies of 0.63 eV, 1.01 eV, and 0.29 eV, respectively. The doping of Mn (Mn^{2+}/Mn^{3+}) at Zn^{2+} site leads to charge compensation mechanism by equation (5) and (6).

Table 4: Activation energy in different temperature ranges, DC conductivity of all samples.

Sample	Activation energy obtained in different regions (eV)			DC conductivity at 500°C (S-cm ⁻¹)
	R-1	R-2	R-3	
ZF-0	0.87	--	--	0.00317
ZF-2	0.45	0.74	--	0.00812
ZF-4	0.63	1.01	0.29	0.00053

In ZF-4, the activation energy of R-3 has lowest, R-2 has highest while R-1 lies in between R-2 and R-3. In order to understand the conduction mechanism involved in ZF-4 sample, the following points should be kept in mind;

- (i) The presence of Mn³⁺ at Zn²⁺ leads to generation of electrons to compensate the overall charge (see equation (6)). It is worthwhile to report that the migration of electrons needs a much lower amount of activation energy i.e., less than 0.5 eV [6]. Based on this, it has been assigned to the conduction of electrons in R-3.
- (ii) However, the higher value of activation energy observed in R-2 suggests the strong association between the dipole effects ($V_o^{\cdot\cdot} - 2Fe^{2+}_{Fe^{3+}}$) and ($2Mn^{3+}_{Zn^{2+}} - 2Fe^{2+}_{Fe^{3+}}$). The XRD study shows that the unit cell contracts, resulting in a stronger association between these defects than ZF-2. So, it implies that it may need more energy for the migration of these defects than ZF-2.
- (iii) Furthermore, the activation energy observed in R-1 was lower than the activation energy observed in R-2. As the temperature rises, the defect's linkage breaks at a

certain point and it moves independently within the investigated temperature range, compared to ZF-0.

Since the total conductivity is affected not only on charge carrier concentration but also on the mobility of individual charge carrier. The influence of Mn doping on electrical conductivity has been explored by comparing the conductivity at 500°C, and given in Table 4. Table 4 shows that the value of dc conductivity is lowest for ZF-4, highest for ZF-2 and in the middle for ZF-0.

In case of ZF-0, the sample has two kinds of defects are in majority such as $V_o^{\cdot\cdot}$ and e' that contributed in overall conductivity according to equation (11). However, by incorporating Mn into the lattice, the d.c. conductivity of sample ZF-2 was increased; this is because Mn^{2+} does not result in any surplus charge to compensate the overall charge. The majority of charge carrier involved in the conduction in sample ZF-2 are defects such as $V_o^{\cdot\cdot}$, e' and dipole defect $V_o^{\cdot\cdot} - 2Fe^{2+}_{Fe^{3+}'}$. The XRD analysis suggests the expansion of the unit cell for sample ZF-2 (See Table 1) and it avails higher mobility for the conduction of charge carrier and results rise in dc conductivity. Moreover, the contraction in unit cell has been observed for sample ZF-4. Since the dielectric analysis revealed the presence of defects $V_o^{\cdot\cdot}$, e' , $V_o^{\cdot\cdot} - 2Fe^{2+}_{Fe^{3+}'}$ and $(2Mn^{3+}_{Zn^{2+}'}) - 2Fe^{2+}_{Fe^{3+}'}$; thus, the contraction in unit cell resulted in strong association, resulting lower mobility. As a result, the dc conductivity has dropped. The oxide $BaZr_{0.8}X_{0.2}O_{3-\delta}$ (X=Y, Sm, Gd) was synthesized by Irshad et al., for the possible application in proton conducting in IT-SOFCs by combustion route [46]. The prepared materials (BZY, BZSm, and BZGd) were sintered at $T=1150$ °C shows maximum conductivity for BZY $\approx 2.2 \times 10^{-3}$ S/cm. However, the value of d.c. conductivity of present investigated samples was found to be higher than reported. Based on the value of activation energy obtained in present investigation, the present materials can be used as

mixed ionic and electronic conductor (MIECs) and proton conductor application in intermediate temperature solid oxide fuel cell (IT-SOFC).

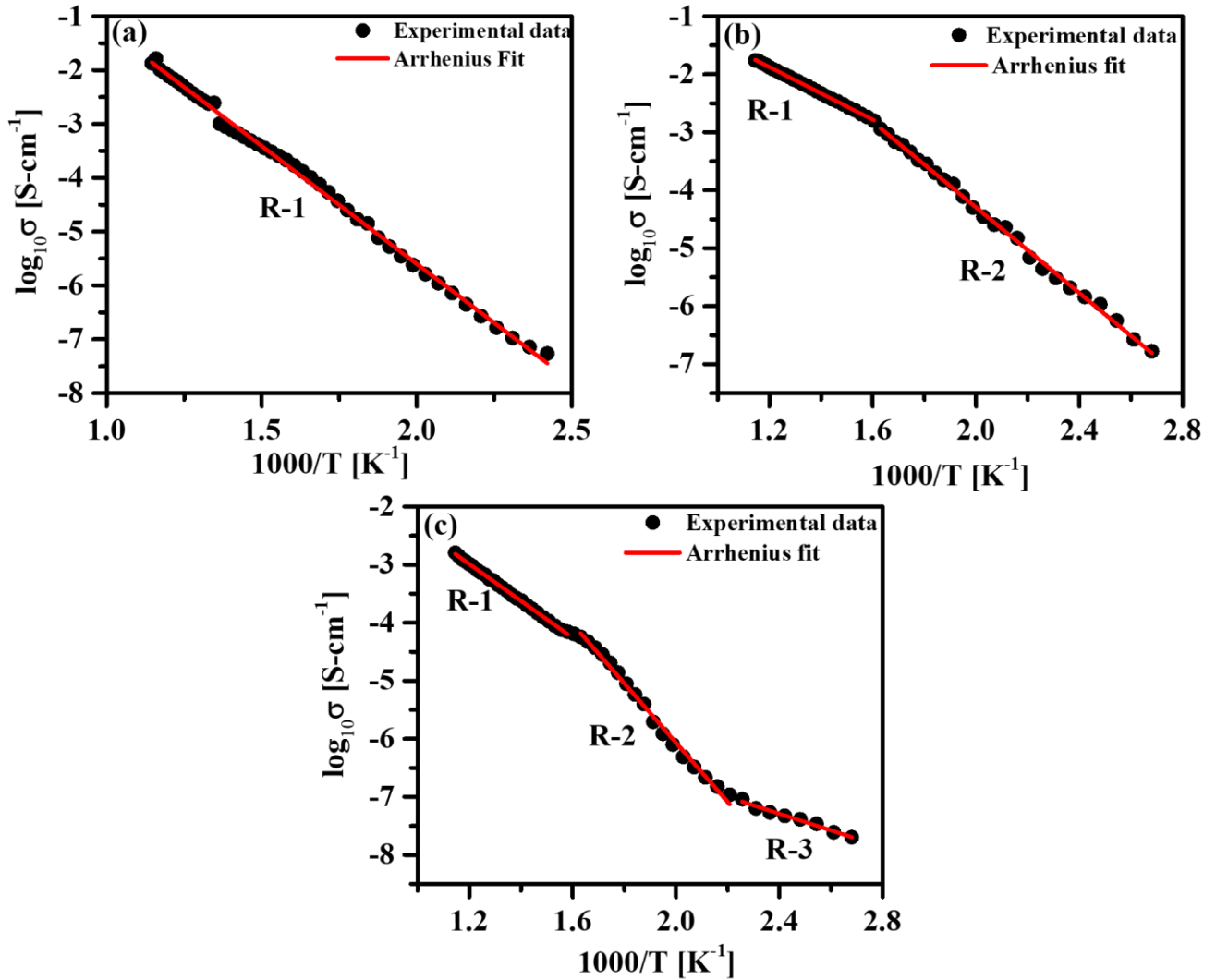


Figure 13: Variation of direct current (DC) conductivity (σ) with inverse of temperature of (a) ZF-0, (b) ZF-2, (c) ZF-4 sample.

Conclusions:

The samples $Zn_{1-x}Mn_xFe_2O_4$ ($x=0, 0.02, 0.04$) were prepared successfully by sol-gel chemical route at 80°C. The XRD analysis of all samples indicates the formation of a single phase. Further, the crystallite size and micro-strain of samples have been studied using W-H plot and

SSP plot. The value of crystallite size found to be highest for ZF-2, lowest for ZF-0 and in middle for ZF-4, while micro-strain gradually increased. The zeta potential of all samples suggests the presence of a positive defect at the surface of the samples. The optical bandgap of samples reflects semiconducting nature. Further the electrical properties of all samples were studied as a function of frequency (1 KHz, 10 KHz, 100 KHz, and 1 MHz) from temperature range 50 to 600°C. The dielectric constant and dissipation factor were found to be increased with temperature while it decreased with frequency. However, the value of dielectric constant found to be lowest for ZF-2 and again increased for ZF-4, while the dissipation factor was not changed significantly with substitution. Moreover, the dc conductivity was found to be highest for ZF-2 and lowest for ZF-4 while it is in middle for ZF-0. The major source of charge carrier for the conduction of defects within the samples are $V_o^{\cdot\cdot}$, e' and dipole defects ($V_o^{\cdot\cdot} - 2Fe^{2+}_{Fe^{3+}}$), ($2Mn^{3+}_{Zn^{2+}} - 2Fe^{2+}_{Fe^{3+}}$). Based on the present study, the present materials can be used for semiconductor devices, proton conductor, and mixed ionic and electronic conductor for IT-SOFCs application.

Declaration of Competing Interest

The authors declare that they have no known competing financial interests or personal relationships that could have appeared to influence the work reported in this paper.

Acknowledgment

Authors are also thankful to DST, Govt. of India, New Delhi, for providing the support in terms of CURIE scheme.

References

1. El Hiti MA (1995) DC conductivity for $\text{Ni}_x\text{Mg}_{1-x}\text{Fe}_2\text{O}_4$ ferrites. *Phase Transitions* 54:117–122. <https://doi.org/10.1080/01411599508213222>
2. Almessiere MA, Slimani Y, Güngüneş H, et al (2020) Impact of Eu^{3+} ion substitution on structural, magnetic and microwave traits of Ni–Cu–Zn spinel ferrites. *Ceram Int* 46:11124–11131. <https://doi.org/10.1016/j.ceramint.2020.01.132>
3. Routray KL, Sanyal D, Behera D (2017) Dielectric, magnetic, ferroelectric, and Mossbauer properties of bismuth substituted nanosized cobalt ferrites through glycine nitrate synthesis method. *J Appl Phys* 122:224104
4. Jia Y, Lee BW, Liu C (2016) Magnetic ZnFe_2O_4 Nanocubes: Synthesis and Photocatalytic Activity With Visible Light/H₂O₂. *IEEE Trans Magn* 53:1–5
5. Passerini L (1930) Ricerche sugli spinelli. II. I composti: CuAl_2O_4 ; MgAl_2O_4 ; MgFe_2O_4 ; ZnAl_2O_4 ; ZnCr_2O_4 ; ZnFe_2O_4 ; MnFe_2O_4 . *Gazz Chim Ital* 60:389–399
6. Cheema H, Kumar S, Alvi PA, et al (2020) Synthesis and physical properties of nanopowder and electrical properties of bulk samples of $\text{ZnFe}_{2-x}\text{Ni}_x\text{O}_4$ (x: 0, 0.05, 0.10). *Adv Powder Technol* 31:4241–4252. <https://doi.org/10.1016/j.appt.2020.09.001>
7. Srivastava R, Yadav BC (2015) Nanostructured ZnFe_2O_4 thick film as room temperature liquefied petroleum gas sensor. *J Exp Nanosci* 10:703–717. <https://doi.org/10.1080/17458080.2013.880001>
8. Zhou X, Liu J, Wang C, et al (2015) Highly sensitive acetone gas sensor based on porous ZnFe_2O_4 nanospheres. *Sensors Actuators B Chem* 206:577–583. <https://doi.org/10.1016/j.snb.2014.09.080>
9. Jiang B, Han C, Li B, et al (2016) In-situ crafting of ZnFe_2O_4 nanoparticles impregnated within continuous carbon network as advanced anode materials. *ACS Nano* 10:2728–2735
10. Li F, Zhan W, Su Y, et al (2020) Achieving excellent electromagnetic wave absorption of ZnFe_2O_4 @ CNT/polyvinylidene fluoride flexible composite membranes by adjusting processing conditions. *Compos Part A Appl Sci Manuf* 133:105866
11. Vadiyar MM, Patil SK, Bhise SC, et al (2015) Improved Electrochemical Performance of a ZnFe_2O_4 Nanoflake-Based Supercapacitor Electrode by Using Thiocyanate-Functionalized Ionic Liquid Electrolytes. *Eur J Inorg Chem* 2015:5832–5838. <https://doi.org/10.1002/ejic.201500870>

12. Vignesh RH, Sankar KV, Amaresh S, et al (2015) Synthesis and characterization of MnFe_2O_4 nanoparticles for impedometric ammonia gas sensor. *Sensors Actuators B Chem* 220:50–58
13. Manohar A, Krishnamoorthi C (2017) Site selective Cu^{2+} substitution in single crystal Fe_3O_4 biocompatible nanospheres by solvothermal reflux method. *J Cryst Growth* 473:66–74. <https://doi.org/10.1016/j.jcrysgro.2017.05.013>
14. Ashok A, Ratnaji T, Kennedy LJ, Vijaya JJ (2020) Magnetically separable $\text{Zn}_{1-x}\text{Cu}_x\text{Fe}_2\text{O}_4$ ($0 \leq x \leq 0.5$) nanocatalysts for the transesterification of waste cooking oil. *Adv Powder Technol* 31:2573–2585
15. Ansari MMN, Khan S (2017) Structural, electrical and optical properties of sol-gel synthesized cobalt substituted MnFe_2O_4 nanoparticles. *Phys B Condens Matter* 520:21–27
16. Zawar S, Atiq S, Tabasum M, et al (2019) Highly stable dielectric frequency response of chemically synthesized Mn-substituted ZnFe_2O_4 . *J Saudi Chem Soc* 23:417–426
17. Hema E, Manikandan A, Gayathri M, et al (2016) The role of Mn^{2+} -doping on structural, morphological, optical, magnetic and catalytic properties of spinel ZnFe_2O_4 nanoparticles. *J Nanosci Nanotechnol* 16:5929–5943
18. Zhao Y, An H, Dong G, et al (2020) Elevated removal of di-n-butyl phthalate by catalytic ozonation over magnetic Mn-doped ferrosinzel ZnFe_2O_4 materials: Efficiency and mechanism. *Appl Surf Sci* 505:144476
19. Raland RD, Borah JP (2016) Efficacy of heat generation in CTAB coated Mn doped ZnFe_2O_4 nanoparticles for magnetic hyperthermia. *J Phys D Appl Phys* 50:35001
20. Tang X, Hou X, Yao L, et al (2014) Mn-doped ZnFe_2O_4 nanoparticles with enhanced performances as anode materials for lithium ion batteries. *Mater Res Bull* 57:127–134. <https://doi.org/10.1016/j.materresbull.2014.05.038>
21. Hakimyfard A, Mohammadi S (2019) ZnFe_2O_4 and $\text{ZnO-Zn}_{1-x}\text{M}_x\text{Fe}_2\text{O}_{4+\delta}$ ($\text{M} = \text{Sm}^{3+}$, Eu^{3+} and Ho^{3+}): Synthesis, physical properties and high performance visible light induced photocatalytic degradation of malachite green. *Adv Powder Technol* 30:1257–1268. <https://doi.org/10.1016/j.appt.2019.04.005>
22. Sagayaraj R, Aravazhi S, Praveen P, Chandrasekaran G (2018) Structural, morphological and magnetic characters of PVP coated ZnFe_2O_4 nanoparticles. *J Mater Sci Mater Electron* 29:2151–2158

23. Liu C, Zou B, Rondinone AJ, Zhang ZJ (2000) Reverse micelle synthesis and characterization of superparamagnetic MnFe_2O_4 spinel ferrite nanocrystallites. *J Phys Chem B* 104:1141–1145
24. Wang L, McCarthy A, Takeuchi KJ, et al (2018) A Combined Experimental and Theoretical Study of Lithiation Mechanism in ZnFe_2O_4 Anode Materials. *MRS Adv* 3:773–778
25. Dhiman M, Sharma R, Kumar V, Singhal S (2016) Morphology controlled hydrothermal synthesis and photocatalytic properties of ZnFe_2O_4 nanostructures. *Ceram Int* 42:12594–12605
26. Hofmann M, Campbell SJ, Ehrhardt H, Feyerherm R (2004) The magnetic behaviour of nanostructured zinc ferrite. *J Mater Sci* 39:5057–5065
27. Tanaka K, Makita M, Shimizugawa Y, et al (1998) Structure and high magnetization of rapidly quenched zinc ferrite. *J Phys Chem Solids* 59:1611–1618
28. Li S, Liu Q, Liu R, et al (2017) Removal performance of methyl blue onto magnetic ZnFe_2O_4 nanoparticles prepared via the solution combustion process. *J Nanosci Nanotechnol* 17:4112–4118
29. Vinosha PA, Mely LA, Jeronsia JE, et al (2017) Synthesis and properties of spinel ZnFe_2O_4 nanoparticles by facile co-precipitation route. *Optik (Stuttg)* 134:99–108
30. Lakshmi M, Kumar KV, Thyagarajan K (2015) An investigation of structural and magnetic properties of Cr–Zn ferrite nanoparticles prepared by a sol–gel process. *J Nanostructure Chem* 5:365–373
31. Shannon RD (1976) Revised effective ionic radii and systematic studies of interatomic distances in halides and chalcogenides. *Acta Crystallogr Sect A* 32:751–767. <https://doi.org/10.1107/S0567739476001551>
32. Kumar U, Upadhyay S (2019) Structural, Optical and Electrical Properties of Ruddlesden Popper Oxide Ba_2SnO_4 . *J Electron Mater* 48:5279–5293. <https://doi.org/10.1007/s11664-019-07336-x>
33. Kumar U, Ansaree MJ, Verma AK, et al (2017) Oxygen vacancy induced electrical conduction and room temperature ferromagnetism in system $\text{BaSn}_{1-x}\text{Ni}_x\text{O}_3$ ($0 < x < 0.20$). *Mater Res Express* 4:116304. <https://doi.org/10.1088/2053-1591/aa9416>
34. Gopi CVVM, Vinodh R, Sambasivam S, et al (2020) Co_9S_8 - Ni_3S_2 / CuMn_2O_4 - NiMn_2O_4

and $\text{MnFe}_2\text{O}_4\text{-ZnFe}_2\text{O}_4/\text{graphene}$ as binder-free cathode and anode materials for high energy density supercapacitors. *Chem Eng J* 381:122640

35. Kumar A, Khan B, Singh G, et al (2020) Structural, microstructure, optical, and electrical properties of Ti-doped CaSnO_3 prepared by Sol-Gel chemical route. *Phys Scr* 95:105807. <https://doi.org/10.1088/1402-4896/abb89f>
36. Kumar U, Upadhyay S (2020) Structural, microstructure, optical, and dielectric properties of $\text{Sr}_{1.99}\text{M}_{0.01}\text{SnO}_4$ (M: La, Nd, Eu) Ruddlesden–Popper oxide. *J Mater Sci Mater Electron* 31:5721–5730. <https://doi.org/10.1007/s10854-020-03140-0>
37. Kumar A, Khan B, Yadav V, et al (2020) Rietveld refinement, optical, dielectric and ac conductivity studies of Ba-doped SrSnO_3 . *J Mater Sci Mater Electron* 31:16838–16848. <https://doi.org/10.1007/s10854-020-04240-7>
38. Kumar U, Yadav D, Upadhyay S (2020) Investigation of structural, optical, and magnetic properties of Nd-doped Sr_2SnO_4 Ruddlesden Popper oxide. *J Am Ceram Soc* 103:5743–5757. <https://doi.org/10.1111/jace.17303>
39. Boschini F, Rulmont A, Cloots R, Moreno R (2009) Rheological behaviour of BaZrO_3 suspensions in non-aqueous media. *Ceram Int* 35:1007–1013. <https://doi.org/10.1016/j.ceramint.2008.04.012>
40. Xu Y, Qin Y, Palchoudhury S, Bao Y (2011) Water-soluble iron oxide nanoparticles with high stability and selective surface functionality. *Langmuir* 27:8990–8997. <https://doi.org/10.1021/la201652h>
41. Gavilán H, Kowalski A, Heinke D, et al (2017) Colloidal Flower-Shaped Iron Oxide Nanoparticles: Synthesis Strategies and Coatings. *Part Part Syst Charact* 34:1700094. <https://doi.org/10.1002/ppsc.201700094>
42. Galinetto P, Albini B, Bini M, Mozzati MC (2018) Raman Spectroscopy in Zinc Ferrites Nanoparticles. *Raman Spectrosc* 223
43. Manohar A, Krishnamoorthi C, Naidu KCB, Pavithra C (2019) Dielectric, magnetic hyperthermia, and photocatalytic properties of ZnFe_2O_4 nanoparticles synthesized by solvothermal reflux method. *Appl Phys A Mater Sci Process* 125:477. <https://doi.org/10.1007/s00339-019-2760-0>
44. Kumar U, Yadav D, Thakur AK, et al (2019) Investigation on phase formation of Sr_2SnO_4 and effect of La-doping on its structural and optical properties. *J Therm Anal Calorim*

- 135:1987–1999. <https://doi.org/10.1007/s10973-018-7432-3>
45. Kumar U, Ansaree J, Upadhyay S (2017) Structural and optical characterizations of BaSnO₃ nanopowder synthesized by aqueous sol-gel method. *Process Appl Ceram* 11:177–184
 46. Irshad M, ul Ain Q, Siraj K, et al (2020) Evaluation of BaZr_{0.8}X_{0.2}O₃ (X= Y, Gd, Sm) proton conducting electrolytes sintered at low temperature for IT-SOFC synthesized by cost effective combustion method. *J Alloys Compd* 815:152389
 47. Kumar U, Upadhyay S (2020) Sr₂SnO₄ Ruddlesden Popper Oxide: Future Material for Renewable Energy Applications. Wiley Online Library
 48. Deotale AJ, Nandedkar R V. (2016) Correlation between Particle Size, Strain and Band Gap of Iron Oxide Nanoparticles. *Mater Today Proc* 3:2069–2076. <https://doi.org/10.1016/j.matpr.2016.04.110>
 49. Nair SS, Mathews M, Anantharaman MR (2005) Evidence for blueshift by weak exciton confinement and tuning of bandgap in superparamagnetic nanocomposites. *Chem Phys Lett* 406:398–403. <https://doi.org/10.1016/j.cplett.2005.02.107>
 50. Kumar U, Upadhyay S (2019) Investigation of structural, optical and electrical properties of Sr₂SnO₄, Sr_{1.99}Eu_{0.01}SnO₄ and Sr₂Sn_{0.99}Eu_{0.01}O₄ Ruddlesden Popper oxide. *Mater Res Express* 6:055805. <https://doi.org/10.1088/2053-1591/aaf2d8>
 51. Callister WD (1991) *Materials science and engineering: An introduction* (2nd edition). *Mater Des* 12:59. [https://doi.org/10.1016/0261-3069\(91\)90101-9](https://doi.org/10.1016/0261-3069(91)90101-9)
 52. JAFFE H (1958) Piezoelectric Ceramics. *J Am Ceram Soc* 41:494–498. <https://doi.org/10.1111/j.1151-2916.1958.tb12903.x>
 53. Kao KC (2004) *Dielectric Phenomena in Solids*
 54. Kumar U, Ankur K, Yadav D, Upadhyay S (2020) Synthesis and characterization of Ruddlesden-Popper system (Ba_{1-x}Sr_x)₂SnO₄. *Mater Charact* 162:110198. <https://doi.org/10.1016/j.matchar.2020.110198>
 55. Yadav D, Kumar U, Nirala G, et al (2019) Effect of acceptor Na¹⁺ doping on the properties of perovskite SrCeO₃. *J Mater Sci Mater Electron* 30:15772–15785. <https://doi.org/10.1007/s10854-019-01963-0>
 56. Yousuf MA, Hussain S, Kousar T, et al (2021) The Impact of pH on Structural and Electrical Properties of Er-Substituted ZnFe₂O₄ Nanoparticles Synthesized via Wet

Chemical Route. *J Supercond Nov Magn* 1–9

57. Mohanty D, Mallick P, Biswal SK, et al (2020) Investigation of structural, dielectric and electrical properties of ZnFe₂O₄ composite. *Mater Today Proc*
58. Sivakumar N, Narayanasamy A, Ponpandian N, Govindaraj G (2007) Grain size effect on the dielectric behavior of nanostructured Ni_{0.5}Zn_{0.5}Fe₂O₄. *J Appl Phys* 101:84116
59. Kumbhar SS, Mahadik MA, Shinde SS, et al (2015) Fabrication of ZnFe₂O₄ films and its application in photoelectrocatalytic degradation of salicylic acid. *J Photochem Photobiol B Biol* 142:118–123
60. Kumar U, Upadhyay S (2018) Studies on dielectric and electrical properties of Ruddlesden-Popper oxide Sr₂SnO₄. *Mater Lett* 227:100–103. <https://doi.org/10.1016/j.matlet.2018.05.046>
61. Yadav D, Kumar U, Upadhyay S (2019) Study of structural, electrical, and photoluminescent properties of SrCeO₃ and Sr₂CeO₄. *J Adv Ceram* 8:377–388. <https://doi.org/10.1007/s40145-019-0320-x>